# Pre-impact dynamics of a droplet impinging on a deformable surface

Nathaniel I. J. Henman, Frank T. Smith and Manish K. Tiwari

View Online          Export Citation          CrossMark

**ARTICLES YOU MAY BE INTERESTED IN**

# Pre-impact dynamics of a droplet impinging on a deformable surface

View Online   Export Citation   CrossMark

Nathaniel I. J. Henman,[1,2] (iD) Frank T. Smith,[2,a)] and Manish K. Tiwari[1,3,b)] (iD)

## AFFILIATIONS

[1] Nanoengineered Systems Laboratory, Department of Mechanical Engineering, University College London (UCL), London, United Kingdom
[2] Department of Mathematics, University College London, London, United Kingdom
[3] Wellcome/EPSRC Centre for Interventional and Surgical Sciences (WEISS), University College London, London, United Kingdom

[a)] Electronic mail: f.smith@ucl.ac.uk
[b)] Author to whom correspondence should be addressed: m.tiwari@ucl.ac.uk

## ABSTRACT

The nonlinear interaction between air and a water droplet just prior to a high-speed impingement on a surface is a phenomenon that has been researched extensively and occurs in a number of industrial settings. The role that the surface deformation plays in an air cushioned impact of a liquid droplet is considered here. In a two-dimensional framework, assuming small density and viscosity ratios between the air and the liquid, a reduced system of integrodifferential equations is derived governing the liquid droplet free-surface shape, the pressure in the thin air film, and the deformation of the surface, assuming the effects of surface tension, compressibility, and gravity to be negligible. The deformation of the surface is first described in a rather general form, based on previous membrane-type models. The coupled system is then investigated in two cases: a soft viscoelastic case where the surface stiffness and (viscous) damping are considered and a more general flexible surface where all relevant parameters are retained. Numerical solutions are presented, highlighting a number of key consequences of surface deformability on the pre-impact phase of droplet impact, such as reduction in pressure buildup, increased air entrapment, and considerable delay to touchdown. Connections (including subtle dependence of the size of entrapped air on the droplet velocity, reduced pressure peaks, and droplet gliding) with recent experiments and a large deformation analysis are also presented.

## I. INTRODUCTION

The impact of a droplet on a deformable surface is a commonly occurring event in a number of industrial and natural settings, such as in anti-icing technologies,[1] ink-jet printing,[2] and rain-induced foliar disease transmission.[3] The use of surface engineering to control droplet impacts[4,5] can have hugely desirable effects in all the applications mentioned above, among others. The main forms of surface engineering revolve around the use of microstructured roughness[6] or textured surfaces,[7] but the aim of this paper is to examine the influence of another alterable surface property, deformability. There have been a number of experimental studies on droplet impacts with flexible, or soft deformable, substrates, considering both the pre-impact[8,9] and post-impact behaviors.[10–12] There has also been some analytical work on the post-impact behavior[13–15] and the pre-impact dynamics of droplet settling,[16] whereas the novelty in our work lies in analyzing the pre-impact behavior of a high-speed droplet impact with a deformable surface.

When considering droplet impacts, the pre-impact air cushioning is an important feature to consider. The high pressures caused by the thin air layer as the droplet approaches a surface are sufficient enough to significantly deform the droplet before impact. Experimental evidence of this can be seen in Lesser and Field[17] and Liow,[18] as well as in Thoroddsen et al.[19] using high-speed photography. All these studies were on flat rigid surfaces and showed that the free-surface distortion prior to impact was significant enough to entrap a small pocket of air underneath the droplet. This experimental work was further extended by Langley et al.[8] to that of impacts with soft deformable solids, and it was found that these impacts entrapped more air than those on rigid surfaces. Mitra et al.[9] then showed that this increased air entrapment of soft solids, and thus extended lifetime of the air layer, facilitates bouncing behaviors of droplets at low-impact velocity and can also significantly influence the air film rupture dynamics. The role of entrapped air under a rebounding droplet impacting on a soft

surface was also considered in Chen et al.[20,21] and attributed to increasing the threshold velocity for a droplet to rebound on softer solids.

A number of theoretical studies consider air cushioning in droplet impacts, in particular Smith et al.[22] who considered a balancing between the forces of an inviscid droplet approaching a rigid wall with a thin, lubricating air layer in between. This rational viscous–inviscid interaction work was further extended by Hicks and Purvis[23–25] for three-dimensional impacts, impacts with liquid layers and other droplets is one paper. Also, Purvis and Smith[26] considered the effect of surface tension and Mandre et al.,[27] Mani et al.,[28] Hicks and Purvis[29] considered the compressibility of the air. More recently, the problem has been considered using axisymmetric direct numerical simulation, in order to have stronger connections with experiments and to explore parameter regimes and other physical effects perhaps not accessible to the inviscid/lubrication model. Wang et al.[30] performed simulations over a large range of impact parameters, identifying different outcomes of both the gas cushioning and post-impact phase of droplet impact. Similarly, Jian et al.[31] examined how variations in the liquid–gas viscosity and density ratios affect the gas cushioning and result in significantly different splashing behaviors. Other works include air cushioning on an immiscible liquid film,[32] heat transfer considerations,[33] and air mediated droplet bouncing.[34] A detailed analytical and numerical study of air entrapment on deformable solid surfaces to complement experimental work[8,9] remains untackled, however.

Liquid–elastic impacts are also the subject of a large number of studies. For example, on an inviscid basis, Korobkin and Khabakhpasheva[35] studied the impact of a regular wave on an elastic plate, and Khabakhpasheva and Korobkin[36] considered a liquid elastic-wedge impact. Similarly, Duchemin and Vandenberghe[37] investigated the impact of a rigid body on a floating elastic membrane. Of most relevance here are droplet-elastic impacts or droplet impacts with flexible surfaces. Pegg et al.[13] investigated the post-impact interactions of a droplet impact on an elastic plate, where it was assumed that the plate had a relatively high rigidity so that it would vibrate, rather than just be deformed by the impact. They used an axisymmetric Wagner-style model of a droplet impact, which was solved using the method of normal modes. They found that the presence of substrate elasticity acted to slow down the velocity of the advancing contact line and that the induced oscillations of the substrate lead to the onset of splashing. Using a similar approach, the effect of surface vibrations was examined in more detail by Khabakhpasheva and Korobkin.[38] Also using post-impact axisymmetric Wagner theory, Negus et al.[15] recently investigated droplet impact on a spring-supported plate, where they found solutions for the composite pressure and force on the plate, and provided an excellent comparison to results obtained via direct numerical simulation. Xiong et al.[14] performed numerical simulations of a droplet impacting a flexible surface using a Lattice–Boltzmann method, investigating the effect of bending stiffness on the contact time and wettability of the droplet on the surface.

There has also been a significant focus on the experimental research on droplet impacts with deformable elastic/flexible surfaces, which has motivated the use of flexible elements in surface engineering and microfluidic devices.[39] Early work by Pepper et al.[40] examined the droplet impact on the elastic membranes of variable tension. They found that by sufficiently lowering the membrane tension, splashing could be suppressed. This work was further complemented by

Howland et al.[12] who investigated the impact of ethanol drops on silicone gels of different stiffnesses, where it was found that the stiffness affects the droplet splashing threshold and could also eliminate splashing all together. In both of these works on splashing, it was suggested that very early times after, even prior to, impact were critical in the overall outcome of the droplet impact. Weisensee et al.[10] considered the droplet impacts with elastic superhydrophobic surfaces and found that the elasticity of the surface was an additional mechanism for reducing the contact time of a bouncing droplet. Vasileiou et al.[11] came to similar conclusions, and Vasileiou et al.[41] found, by investigating the impacts with supercooled droplets, that substrate flexibility can improve the icephobicity. Similarly, a detailed study of the dynamics of the flexible superhydrophobic surface by a droplet impact was performed by Kim et al.[42] The studies discussed here are typically based on the deformable substrate coatings or clamped-clamped membrane designs; however, droplet impact on the cantilever designed surfaces has also received attention.[10,43,44]

The focus of the present study is on an analytical and numerical investigation into the pre-impact behavior of a droplet impacting a deformable surface. Understanding the pre-impact behavior of the droplet is vital in understanding the post-impact behavior. Although in practice droplet impacts are three-dimensional, we will formulate a simplified two-dimensional model and we will use our study to try to gain a qualitative understanding of the effect of surface deformation on various impact quantities, such as touchdown time, contact pressure, and air entrapment, which play an important role in understanding the effect on splashing, spreading and wettability of the droplet post-impact (we note a recent very interesting study by Pegg[45] on elastic surfaces which has some overlap with ours). In Sec. II, we formally define the problem and describe an asymptotic analysis which allows us to define a reduced set of governing equations for the droplet free-surface, the pressure in the air film and the shape of the surface as they evolve and interact. We choose to model the deformable surface by the compliant surface model of Carpenter and Garrad[46] which includes rigidity, tension, stiffness, inertia, and damping and so is representative of a number of different surfaces. The aim of this study is to assess the influence of each of these physical parameters. In Secs. III and IV, we then numerically investigate the solutions, by performing a parametric study of the parameters of the surface. Connections with the experiments are then addressed in Sec. V. In Sec. VI, we consider the interesting case of relatively large surface deformations, which points to another link with experiments concerning droplet gliding, while Sec. VII presents the conclusions.

## II. MODEL FORMULATION AND GOVERNING EQUATIONS

Suppose a two-dimensional liquid droplet of radius $R$ approaches a deformable surface with normal velocity $V$. Initially, the droplet will be sufficiently far away from the surface that the pressure between the droplet and the surface is constant and the droplet remains circular. Let $(x^*, y^*)$ be the Cartesian coordinates and $t^*$ be time. Then the bottom free-surface of the droplet will initially be

$$f^*(x^*, t^*) = -\sqrt{R^2 - x^{*2}} - Vt^* + R. \tag{1}$$

The deformable surface will be denoted $g^*(x^*, t^*)$ and undisturbed will lie on $y^* = 0$. Time is measured such that in the absence of air

cushioning, the droplet would impact the undisturbed deformable surface at $t^* = 0$.

The aim is to derive a system of equations that govern the droplet free-surface, the air film pressure between the droplet and the deformable surface, and the shape of the surface. In order to do this, the fluid flow will have to be considered separately in the liquid droplet and the air film and an equation governing the shape deformations of the surface will also be considered. These three quantities will form a coupled system. The following derivation will assume that the effects of surface tension, compressibility, and gravity are negligible, and these assumptions will be discussed in detail later on in this section. The subsequent analysis will exploit the small density ratio $\rho_g \ll \rho_l$, of the liquid ($l$) to the gas ($g$) in order to obtain asymptotically valid equations describing the droplet free-surface, the pressure in the air gap and the shape of the surface. The small quantity used in the asymptotic analysis will be defined as the aspect ratio of the local horizontal length scale $l$, over which the pressure has a leading order effect on the droplet free-surface, to the droplet radius $R$,
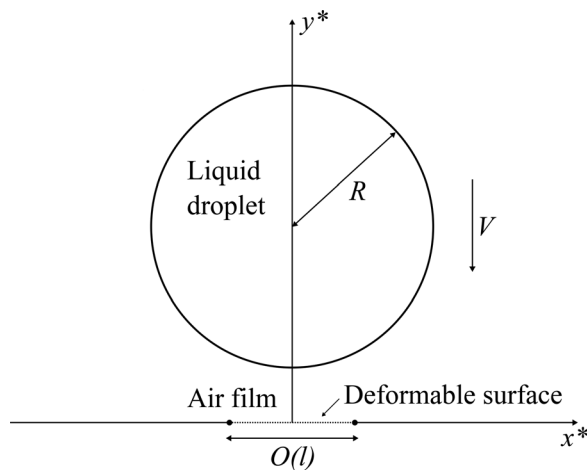
$$\varepsilon = \frac{l}{R}. \tag{2}$$

Here, $l$ is still to be determined. Figure 1 shows a schematic of the problem setup.

All distances are non-dimensionalized with the droplet radius $R$ and time is non-dimensionalized with $R/V$; thus, $(x^*, y^*) = R(x, y)$ and $t^* = Rt/V$. Fluid velocity components in both fluids are non-dimensionalized with $V$ and pressure with $\rho_l V^2$. The flow in the droplet and the air film is assumed to be governed by the incompressible Navier–Stokes equations and using the above notation these are

$$\frac{\partial \boldsymbol{u}_l}{\partial t} + \boldsymbol{u}_l \cdot \nabla \boldsymbol{u}_l = -\nabla p_l + \frac{1}{Re} \nabla^2 \boldsymbol{u}_l, \tag{3a}$$

$$\nabla \cdot \boldsymbol{u}_l = 0, \tag{3b}$$



FIG. 1. Schematic of the model problem of a two-dimensional droplet of radius $R$ approaching a deformable surface of length $O(l)$ with velocity $V$, with an air film in between. $l$ is the horizontal length scale over which the interaction of the liquid and air film takes place. The impact is cushioned by the air film between the droplet and the deformable surface.

for the liquid and

$$\frac{\partial \boldsymbol{u}_g}{\partial t} + \boldsymbol{u}_g \cdot \nabla \boldsymbol{u}_g = -\frac{\rho_l}{\rho_g} \nabla p_l + \frac{\nu_g}{\nu_l} \frac{1}{Re} \nabla^2 \boldsymbol{u}_g, \tag{4a}$$

$$\nabla \cdot \boldsymbol{u}_g = 0, \tag{4b}$$

for the air, where $\nabla = (\partial/\partial x, \partial/\partial y)$, $\nu_\alpha = \mu_\alpha/\rho_\alpha$ is the kinematic viscosity of the liquid ($\alpha = l$) or gas ($\alpha = g$), $\boldsymbol{u}_\alpha = (u_\alpha, v_\alpha)$ is the fluid velocity field, and $Re = RV/\nu_l$ is the global Reynolds number based on the properties and initial velocity of the liquid. For the parameter regime of interest, the Reynolds number $Re$ is typically large, and this will, again, be discussed at the end of this section.

The non-dimensional initial liquid free-surface profile is now given by

$$f(x, t) = -\sqrt{1 - x^2} - t + 1. \tag{5}$$

To close our system, we must satisfy the kinematic boundary conditions on the liquid–gas interface and the gas–surface interface,

$$\frac{\partial f}{\partial t} + u_\alpha \frac{\partial f}{\partial x} = v_\alpha \quad \text{at } y = f(x, t), \tag{6}$$

and

$$\frac{\partial g}{\partial t} + u_\alpha \frac{\partial g}{\partial x} = v_\alpha \quad \text{at } y = g(x, t), \tag{7}$$

for $\alpha = l$ or $g$. Neglecting surface tension effects gives the normal stress balance on the liquid–gas interface as

$$p_l = p_g. \tag{8}$$

Due to the disparate horizontal velocity scales between the liquid and the gas, a tangential stress balance on the liquid–gas interface is not required, as it will be seen later that a no-slip condition is applied on this boundary (this involves a thin shear layer present as in Smith et al.[22]).

## A. Liquid droplet

To determine the behavior of the liquid droplet free-surface, close to the point of initial contact which is $x = y = 0$, we take the following scaling:

$$(x, y, t, f) = (\varepsilon X, \varepsilon Y, \varepsilon^2 T, \varepsilon^2 F), \tag{9}$$

where the scales of $t$ and $f$ come from the desire to study short time behavior and from the form of Eq. (5), respectively. The $O(\varepsilon^2)$ time-scale is that expected for the traversing, at a unit non-dimensional velocity, of the thin air gap which has normal width of $O(\varepsilon^2)$. The scales (9) lead us to take asymptotic expansions of the liquid velocity components and pressure in the following form:

$$(u_l, v_l, p_l) = (U_l, V_l, \varepsilon^{-1} P_l) + \cdots. \tag{10}$$

The vertical velocity scale is order unity due to the order unity downward velocity of the droplet, and then the horizontal velocity scale follows from continuity. The large pressure scale arises from seeking a balance between the liquid acceleration and the pressure gradient.

Now, for $Re \gg 1$, upon substitution of scales (9) and expansions (10) into the governing equations (3a) and (3b), the leading order

momentum equations and continuity equation are those of unsteady potential flow,

$$\frac{\partial U_l}{\partial T} = -\frac{\partial P_l}{\partial X}, \tag{11a}$$

$$\frac{\partial V_l}{\partial T} = -\frac{\partial P_l}{\partial Y}, \tag{11b}$$

$$\frac{\partial U_l}{\partial X} + \frac{\partial V_l}{\partial Y} = 0. \tag{11c}$$

The leading order kinematic condition (6) now reduces to

$$V_l \to \frac{\partial F}{\partial T}, \quad \text{as } Y \to 0^+, \tag{12}$$

while the far-field droplet behavior reduces to

$$F(X,T) \sim \frac{X^2}{2} - T + O(\varepsilon), \quad \text{as } |X| \to \infty \text{ or } T \to -\infty, \tag{13}$$

from (5).

From Eqs. (11a)–(11c), it can be shown that $P_l$ satisfies Laplace's equation and due to the far-field boundedness (13) and condition (12), the pressure profile on the droplet interface $P(X, T) = P_l(X, 0, T)$ and free-surface profile $F(X, T)$ are related by

$$\frac{\partial^2 F}{\partial T^2} = \frac{1}{\pi}(\text{PV}) \int_{-\infty}^{\infty} \frac{\partial P}{\partial \zeta}(\zeta, T) \frac{d\zeta}{X - \zeta}. \tag{14}$$

Here (PV) denotes the Cauchy principle value integral.

### B. Gas cushioning

In the thin gas film between the droplet and the deformable surface, we assume that the vertical length scale is an order of magnitude smaller than the horizontal length scale to capture the slenderness of the film. Also, unlike in the droplet formulation, we now need to consider the deformable surface $g$, which we supposed to have the same scale as the droplet free-surface $f$ in order for the surface deformation to have a leading order influence. We then take the following scaling in terms of our previously defined small parameter $\varepsilon$:

$$(x, y, t, f, g) = (\varepsilon X, \varepsilon^2 Y, \varepsilon^2 T, \varepsilon^2 F, \varepsilon^2 G). \tag{15}$$

The scales (15) lead to asymptotic expansions of the form

$$(u_g, v_g, p_g) = (\varepsilon^{-1} U_g, V_g, \varepsilon^{-1} P_g) + \cdots, \tag{16}$$

where the horizontal velocity scale is expected to be large compared with the vertical velocity scale in order to balance the continuity equation.

When substituting scales (15) and expansions (16) into the governing equations for the gas (4), for $Re \gg 1$ the leading order equations take the form of lubrication flow,

$$0 = \frac{\partial P_g}{\partial X} + \frac{\partial^2 U_g}{\partial Y^2}, \tag{17a}$$

$$0 = -\frac{\partial P_g}{\partial Y}, \tag{17b}$$

$$\frac{\partial U_g}{\partial X} + \frac{\partial V_g}{\partial Y} = 0. \tag{17c}$$

The inertial and acceleration terms do not appear in the left-hand side of Eqs. (17a) and (17b) because these terms are negligible compared to the pressure gradient term. This assumption requires $\rho_g/\rho_l \ll \varepsilon$. Also, it is assumed that there is a balance in the horizontal momentum equation between the pressure gradient and the viscous terms,[22] which leads to the definition

$$\varepsilon = \left(\frac{\mu_g}{\mu_l Re}\right)^{1/3}. \tag{18}$$

This, combined with the requirement $Re \gg 1$ in the liquid, gives the condition that $\varepsilon$ must satisfy in order for our model to be valid, namely,

$$\frac{\rho_g}{\rho_l} \ll \varepsilon \ll \left(\frac{\mu_g}{\mu_l}\right)^{1/3}. \tag{19}$$

For example, water and air give rise to the range $10^{-3} \ll \varepsilon \ll 0.27$.

The leading order kinematic conditions (6) and (7) now reduce to

$$V_g = \frac{\partial F}{\partial T} \quad \text{at } Y = F(X, T) \tag{20}$$

and

$$V_g = \frac{\partial G}{\partial T} \quad \text{at } Y = G(X, T), \tag{21}$$

respectively. The vertical momentum equation (17b) implies that $P_g(X, Y, T) = P_g(X, 0, T)$, then integrating Eq. (17a) twice in $Y$ and applying conditions (20) and (21), with normal stress condition (8), gives

$$\frac{\partial}{\partial X}\left((F - G)^3 \frac{\partial P}{\partial X}\right) = 12 \frac{\partial}{\partial T}(F - G), \tag{22}$$

the (Reynolds) lubrication equation that helps to link all three unknown quantities $F$, $G$, and $P$.

### C. The deformable surface

Finally, we require another equation linking the pressure in the air film with the deformation of the surface. The model we will use here was first described by Carpenter and Garrad[46] to model surface coatings as an elastic plate (or tensioned membrane) supported above a rigid surface by an array of springs. It is derived from a nonlinear model that includes all relevant physics which is then linearized under the assumption of longitudinal deflections being much smaller than transverse ones. An excellent derivation of this equation can be found in Alexander et al.[47] (we will ignore viscous traction in the air film in our model). This model is also used in a number of other studies on deformable surfaces.[48–52] The relevant equation takes the non-dimensional form

$$e_1 \frac{\partial^4 g}{\partial x^4} + e_2 \frac{\partial^2 g}{\partial x^2} + e_3 g + e_4 \frac{\partial^2 g}{\partial t^2} + e_5 \frac{\partial g}{\partial t} = p(x, g, t) - p_s(x, g, t), \tag{23}$$

where the non-dimensional coefficients $e_i$ are $(e_1, e_2, e_3, e_4, e_5) = (-B^*/R^3 V^2 \rho_l, T_t^*/RV^2 \rho_l, -\kappa^* R/V^2 \rho_l, -M^*/R \rho_l, -C^*/V \rho_l)$ and

$p_s$ is the non-dimensional relative base pressure, which is taken to be zero. We choose to use this thin-membrane type model over simpler models as there is commonality in such membranes in nature and practical settings, such as droplet impact on leaves,[3] butterflies,[53] umbrellas and raincoats, and relevance in many other applications of droplet impact on deformable surfaces discussed elsewhere in this paper. More simple surface deformation models can be extracted as subsets from Eq. (24) and one such, a Kelvin–Voigt model of viscoelasticity, is described in detail in Sec. III while the equation is considered in full generality in Sec. IV. The recent study by Pegg[45] is likewise based on the theory of Smith et al.[22] but with a surface equation generally different from ours; the present work is more focused on soft deformable surfaces which are found to lead to new non-intuitive results. The constants $B^*$, $T_t^*$, $\kappa^*$, $M^*$, and $C^*$ correspond to the flexural rigidity, the longitudinal tension, the stiffness, the mass density and the damping constant of the surface, respectively. In order to apply Eq. (23) to our scaled liquid droplet application described above, we must apply scales for $g$, $x$, $t$, and $p$ given in (15) and (16). This gives

$$\tilde{e}_1 \frac{\partial^4 G}{\partial X^4} + \tilde{e}_2 \frac{\partial^2 G}{\partial X^2} + \tilde{e}_3 G + \tilde{e}_4 \frac{\partial^2 G}{\partial T^2} + \tilde{e}_5 \frac{\partial G}{\partial T} = P - P_s, \quad (24)$$

where $(\tilde{e}_1, \tilde{e}_2, \tilde{e}_3, \tilde{e}_4, \tilde{e}_5) = (\varepsilon^{-1}e_1, \varepsilon e_2, \varepsilon^3 e_3, \varepsilon^{-1}e_4, \varepsilon e_5)$ and $P_s = \varepsilon^{-1}p_s$. Therefore, the five non-dimensional parameters which control the system are the following:

$$\tilde{e}_1 = -\frac{B^*}{(\rho_l^2 \mu_g V^5 R^8)^{1/3}}, \quad \tilde{e}_2 = \frac{T_t^*}{(\rho_l^4 \mu_g^{-1} V^7 R^4)^{1/3}},$$
$$\tilde{e}_3 = -\frac{\kappa^*}{\rho_l^2 \mu_g^{-1} V^3}, \quad \tilde{e}_4 = -\frac{M^*}{(\rho_l^2 \mu_g V^{-1} R^2)^{1/3}}, \quad (25)$$
$$\tilde{e}_5 = -\frac{C^*}{(\rho_l^4 \mu_g^{-1} V^4 R)^{1/3}}.$$

The relative size and importance of each term will be discussed in each case considered in this study. In practice, each of the structural parameters $B^*$, $T_t^*$, $\kappa^*$, $M^*$, and $C^*$ can vary dramatically depending on the situation, so therefore so can each $e_i$ in (25). As droplet impact is a ubiquitous phenomenon, it can occur on many different surfaces of differing elastic properties, for example, leaves,[3] thin foils,[54] skin,[55] and foodstuffs.[56] It is also possible to use surface engineering to modify the elastic properties of a surface to our advantage.[8,10–12,41] Therefore, our focus will be on studying different cases of Eq. (24), with a very wide range of values of the parameters $e_i$.

The deformable surface will be considered to be initially zero and stationary. Boundary conditions will be discussed separately for each case considered. The system to be solved is the nonlinear set of governing equations (14), (22), and (24), subject to the boundary condition (13), the pressure $P$ being initially zero and decaying at infinity, and the relevant boundary and initial condition on $G$. The governing equations require a numerical treatment. The numerical scheme is slightly different for each case considered and so will be discussed separately for each case.

### D. Fluid parameter regime and model validity

It is useful now to mention the fluid parameters used in recent experiments. Of most relevance here, we will consider the experiments performed by Langley et al.[8] for the pre-impact behavior of ethanol droplets impacting soft surfaces of varying stiffness. They considered a parameter regime where the Reynolds number $Re$ ranged from 1209 to 20 394 and the Weber number $We$ ranged from 17 to 2825. Hence, both are typically large and, in particular, the assumption of a quasi-inviscid liquid droplet seems valid in this regime. Also, in the present study surface tension has been ignored and the scaled surface tension forces are given by

$$\frac{\varepsilon^2}{\rho_l V^2 l} \sigma \nabla^2 F = \frac{\varepsilon}{We} \nabla^2 F, \quad (26)$$

where $\sigma$ is the surface tension coefficient and $We = \rho_l V^2 R/\sigma$ is the Weber number. As the parameter $\varepsilon$ is small and $We$ is typically large, this again seems a valid assumption for the vast majority of the evolution. As the droplet approaches the surface, we do still expect the free-surface to deform to the point where high curvatures are observed, as seen in Smith et al.[22] This would result in a large value for $\nabla^2 F$, and thus surface tension forces may become significant at this stage. However, for some cases in Sec. III the free-surface curvature will not become large at any stage and so surface tension effects remain small. The effect of the surface tension is considered in Purvis and Smith[26] for droplet impacts in our parameter regime and in Vanden-Broeck and Smith[57] for a similar air-cushioning related problem for higher Reynolds numbers than in this work. In the present study, however, as has already been assumed, surface tension effects will be ignored. For all parameters considered in Langley et al.[8] the Froude number $Fr = V/\sqrt{gR}$, where $g$ is the gravitational acceleration, is also large; hence, the gravitational effects are ignored.

The effects of compressibility in the air film are also ignored in the present study. A scaling argument performed by Mandre et al.,[27] where they balanced the gas pressure gradient with the droplet deceleration, found that compressibility effects in the air can be ignored if the compressibility parameter $\delta$ satisfies

$$\delta = \frac{p_0^*}{(R\mu_g^{-1} V^7 \rho_l^4)^{1/3}} \gg 1, \quad (27)$$

where $p_0^*$ is the surrounding ambient pressure. In the study of Langley et al.,[8] there are impacts considered both in the compressible ($\delta < 1$) and incompressible regimes ($\delta \gg 1$), so we will still attempt to draw comparisons with their work later in Sec. V. For detailed discussions of compressible gas-cushioned droplet impacts, see Mani et al.[28] and Hicks and Purvis[29] also.

Figure 2 summarizes the main model assumptions for a water droplet impact, when $p_0^* = 10^5$ Pa. There is a clear and rather large range of droplet velocities and radii where our model is valid, and this is the gray shaded region in Fig. 2, where the cross shows where the droplet radius is 1 mm and the velocity is 1 m s$^{-1}$, a point well within our regime.

## III. IMPACT ON A VISCOELASTIC SOLID

The first case that will be considered is that of an air cushioned droplet impact on a soft viscoelastic solid. The viscoelastic material will be assumed to exhibit no rigidity, tension, or inertia, such as a coating on a rigid surface of infinite horizontal extent. In this case, we may remove the influence of coefficients $\tilde{e}_1$, $\tilde{e}_2$, and $\tilde{e}_4$ [this can be
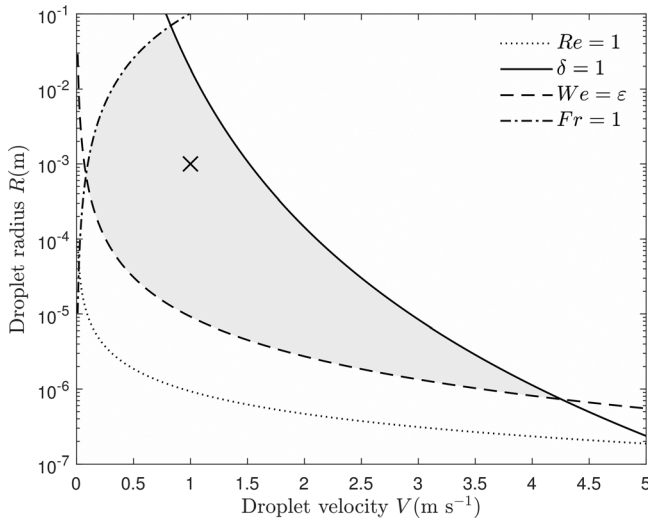
**FIG. 2.** Range of parameter validity for a water droplet impact in air, with $p_0^* = 10^5$ Pa. Above the dotted line $Re \gg 1$ and the liquid droplet may be considered quasi-inviscid, below the solid line $\delta \ll 1$ and compressibility effects in the air may be ignored, above the dashed line $We \gg \varepsilon$ and surface tension forces may be ignored for the vast majority of the evolution, and below the dashed-dotted line $Fr \gg 1$ and gravitational effects may be ignored. These limits are represented by the gray shaded region. The cross is the point where the droplet radius is 1 mm and the droplet velocity is 1 m s$^{-1}$, a set of values well within our regime and used commonly in this paper for dimensional calculations.



**FIG. 3.** Schematic representation of the scaled, non-dimensional problem setup of droplet impact on a viscoelastic solid pre-impact (this is not a solution).
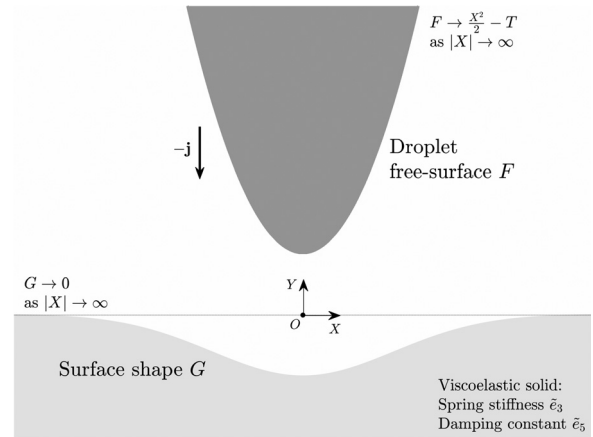
envisaged as removing the influence of the elastic plate, or membrane, from Eq. (24)] and reduce our deformable surface equation (24) to

$$\tilde{e}_3 G + \tilde{e}_5 \frac{\partial G}{\partial T} = P, \qquad (28)$$

which gives the simple Kelvin–Voigt model of a solid deforming in reaction to an applied pressure. Droplet impact and dynamics on soft viscoelastic solids has received attention both experimentally[20,21] and analytically.[58] A schematic of the problem setup is shown in Fig. 3.

If the soft viscoelastic solid is a coating sitting on an otherwise rigid surface, the coating depth would need to be $O(\varepsilon^2 R)$ in order for the depth to have an influence on the dynamics. If $d^*$ is the dimensional depth of the coating, then this can be envisaged as $d^* \ll \varepsilon R$, which for a droplet of radius 1 mm and velocity 1 m s$^{-1}$ becomes $d^* \ll 26\,\mu m$. In the experiments of Howland et al.[12] they predominantly considered soft substrates of depth 1 cm, well outside this limit; however, they did also discuss the effect of a substrate of depth 3 $\mu$m, which is within this limit. It was found that the splashing behavior of the impacting droplet on this very shallow soft silicone substrate was almost identical to that of a much deeper substrate of hard acrylic. In light of this fairly uninteresting behavior for substrates of shallow depth, we will limit our study to the case of surfaces of apparent infinite depth with zero under-pressure ($P_s = 0$). The smallest depth of substrate considered in Langley et al.[8] was 1 mm, also well outside this limit.

Given the form of Eq. (28), it follows naturally that if the pressure is decaying at infinity, then so is the surface deformation. Therefore, the boundary condition at infinity will be $G \to 0$. The viscoelastic model equation (28) is solved in conjunction with the free-surface

equation (14) and the lubrication equation (22). The numerical method proceeds by first substituting Eq. (28) into Eqs. (14) and (22) for $P$. At each time step, the lubrication equation (22) is solved via a finite difference discretization for $G$, which is then used to solve the free-surface equation (14) for $F$, using Fast Fourier Transform algorithms. This process is repeated until successive iterates are within the convergence criteria, after which the solution proceeds to the next time step. Once we have a converged solution for $G$, the pressure $P$ is then readily calculated from Eq. (28). This method is akin to that used in Hicks and Purvis.[25] By eliminating the pressure from our simultaneous equations, the efficiency of the code is improved somewhat as not only do we have two equations to solve as opposed to three, we are no longer having to resolve a diverging pressure solution[22] from the lubrication equation, which can be computationally expensive. Tests were run to ensure the solutions were independent of grid size and time step size. A suitable spatial domain size here was found to be $X \in [-20, 20]$, with the boundaries here being noninvasive and the solutions remaining unchanged for further increases to the spatial domain size. The simulations are very sensitive to the chosen start time. We performed a test on the surface with parameters $(\tilde{e}_1, \tilde{e}_2, \tilde{e}_3, \tilde{e}_4, \tilde{e}_5) = (0, 0, -0.1, 0, -0.1)$ (the most deformable surface considered in this study) with start times of $T = -50$ and $T = -100$. It was found that the difference in the size of entrapped air upon touchdown (defined in Sec. III B) was 2.5% for these two start times, and so $T = -50$ was chosen as the start time for all simulations.

## A. Free-surface and pressure profile evolution

Figure 4 shows the evolution of the droplet free-surface and pressure profile for a flat rigid surface ($G = 0$) and for a viscoelastic surface for a range of values of $\tilde{e}_3 = \tilde{e}_5$. We chose to vary the parameters as $\tilde{e}_3 = \tilde{e}_5$ because, in practice, they are dependent on each other; however, different combinations are considered later on. The top two panels are the solution for a flat rigid surface which has been previously reported a number of times.[22,25] As the droplet approaches the surface, there is an initial buildup of pressure directly beneath the droplet. The buildup of pressure acts to decelerate the falling droplet and as the gap
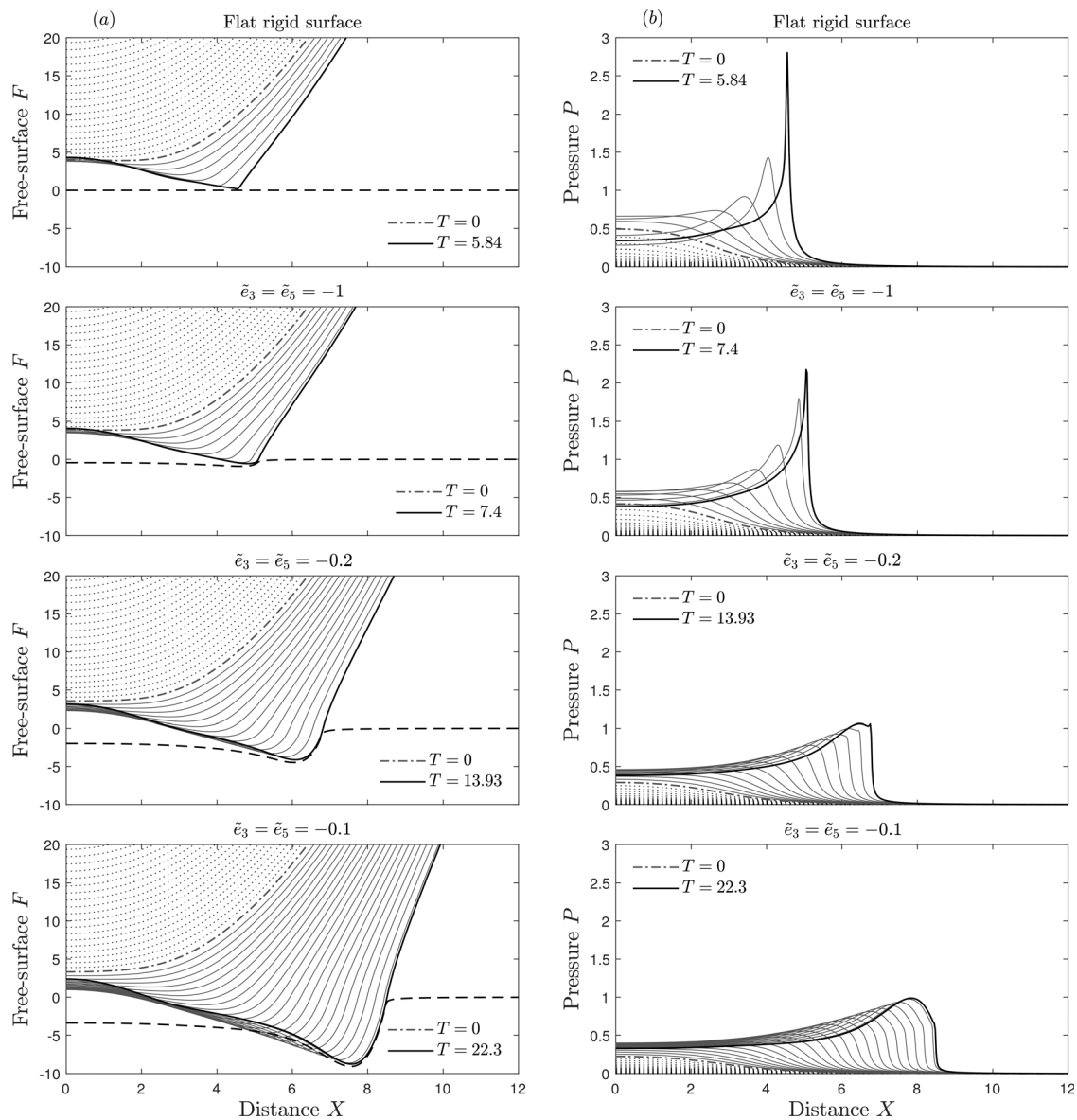
**FIG. 4.** Solution profiles, showing the evolution of (a) the free-surface height $F$ and (b) the pressure $P$ for normal impact of a droplet on a flat rigid surface and deformable viscoelastic surfaces with $\tilde{e}_3 = \tilde{e}_5 = -1$, $-0.2$, and $-0.1$. The solutions are shown in integer time increments except for the final thick solid line, which is the solution just prior to touchdown, and the dashed line, which is the deformable surface solution $G$ just prior to touchdown. The dashed-dotted line is the solution at $T = 0$ where the droplet would touchdown on an undisturbed surface in the absence of air cushioning.

between the droplet and the surface narrows, the pressure buildup is large enough to decelerate the droplet free-surface to rest at the center point. At this stage, the droplet begins to deform either side of the center point and eventually overtake it, resulting in an approach to touchdown in two locations. This, in turn, results in the pressure bifurcating away from the center point into two pressure peaks. The process continues until the moment of touchdown on the surface, which results in the entrapment of an air pocket, which may then subsequently form a bubble.[2,19]

The result for the flat rigid surface in Fig. 4 is then compared to the result for impact on a viscoelastic surface for decreasing magnitudes of the surface parameters $\tilde{e}_3 = \tilde{e}_5$. Lowering the magnitude of the surface parameters $\tilde{e}_3$ and $\tilde{e}_5$ corresponds to lowering the surface stiffness and (viscous) damping, which results in larger surface deformations. Rows two to four in Fig. 4 show the solutions for the free-surface and the pressure profile evolution, along with the shape of the surface as touchdown is approached, for $\tilde{e}_3 = \tilde{e}_5 = -1$, $-0.2$, and $-0.1$, respectively. For a water droplet in air of radius 1 mm and

impact velocity $1 \, \text{m s}^{-1}$, these parameter variations correspond to a surface spring stiffness in the range $\kappa^* \sim 10^9 – 10^{10} \, \text{Pa m}^{-1}$ and (viscous) damping of $C^* \sim 10^3 – 10^4 \, \text{Pa s}$. We note that the spring stiffness values here are larger than the stiffnesses of the soft solids considered in Langley et al.;[8] however, the spring stiffness defined in Eq. (24) is a stiffness *per unit length* and the length scales in this problem are typically very small. Smaller values of the dimensionless parameter $\tilde{e}_3$ are considered in Sec. III B.

A number of conclusions can be drawn from the influence of surface deformability in this viscoelastic model on the pre-impact dynamics of droplet impact. First of all, there is a profound delay to touchdown. In the absence of air cushioning, the droplet would impact on an undisturbed surface at $X = Y = 0$ at $T = 0$. The presence of air cushioning delays this touchdown into positive time. In Fig. 4 the solution at $T = 0$ is the dashed-dotted line, while the positive time solutions are the solid lines. As the droplet approaches the soft viscoelastic surface, the buildup of pressure beneath the droplet acts now to not only deform and decelerate the droplet free-surface but also push the surface away from the droplet. This results in a slower closing of the air gap between the droplet and the soft viscoelastic surface, with lower magnitudes of surface parameters $\tilde{e}_3$ and $\tilde{e}_5$ resulting in a slower closing of the air gap. In consequence there is a larger delay to touchdown as illustrated by the thick solid lines in Fig. 4, corresponding to the solution as touchdown is approached, where the time has increased from $T = 5.84$ for a flat rigid surface to $T = 22.3$ for the soft viscoelastic surface with $\tilde{e}_3 = \tilde{e}_5 = -0.1$. The dimensional timescale is given by

$$t^* = \frac{\varepsilon^2 R}{V} T = \frac{\mu_g^{2/3} R^{1/3}}{\rho_l^{2/3} V^{5/3}} T. \qquad (29)$$

For a 1 mm water droplet in air with impact velocity $1 \, \text{m s}^{-1}$, the touchdown delay incurred here is $11.4 \, \mu s$.

The slower closing of the air gap also influences the buildup of pressure beneath the droplet. In Fig. 4 as the parameters $\tilde{e}_3$ and $\tilde{e}_5$ are decreased in magnitude, the bifurcating behavior of the pressure profiles is still present. However, the pressure peak amplitude as

touchdown is approached is lowered by the introduction of surface deformability, with larger surface deformations resulting in lower pressures.

Figure 5 highlights the link between the rate at which the air gap closes and the maximum pressure. The lower pressures seen for more deformable surfaces are found to be present at all time.

It is also interesting to note the shape of the pressure solution as touchdown is approached. Figure 6 shows the air film thickness $H = F - G$ and pressure profile solution for a range of values $\tilde{e}_3 = \tilde{e}_5$. It can be seen that for surface parameters of sufficiently high magnitude, the pressure profile solution near touchdown is virtually identical to that of the flat surface solution,[22,25] with a very sharp pressure peak located at the cusp of the air film thickness $H$. As the magnitude of the surface parameters is decreased, the sharp pressure peak near touchdown still exists up until around $\tilde{e}_3 = \tilde{e}_5 = -0.2$ (this solution is also shown in Fig. 4) where a rounder pressure peak located just behind the cusp of the air film thickness $H$ is seen. As the magnitude of the surface parameters is decreased further to $\tilde{e}_3 = \tilde{e}_5 = -0.1$, the rounder pressure peak overtakes the sharp one near touchdown. The location of the lower, rounder pressure peak just behind the cusp of the air film thickness, as opposed to at it, could help explain the extended air gliding behavior for droplet impacts on to softer solids seen in experiments by Langley et al.[8] Air gliding is when a droplet skids on a thin air film as opposed to touching down; the numerical solutions of the air film thickness in Fig. 6(a) appear to show the onset of such behavior.

### B. Entrapped air size

A vitally important outcome of the dynamics described here is the area of entrapped air underneath the droplet at impact. Trapped air at impact can cause potential problems when it comes to using droplets to spray coat materials or in cooling processes. From the numerical results of pre-impact air–water–surface interaction in Fig. 4 it is clear that air entrapment still occurs. What is perhaps more clear in Fig. 6 is that the presence of surface deformability in the viscoelastic
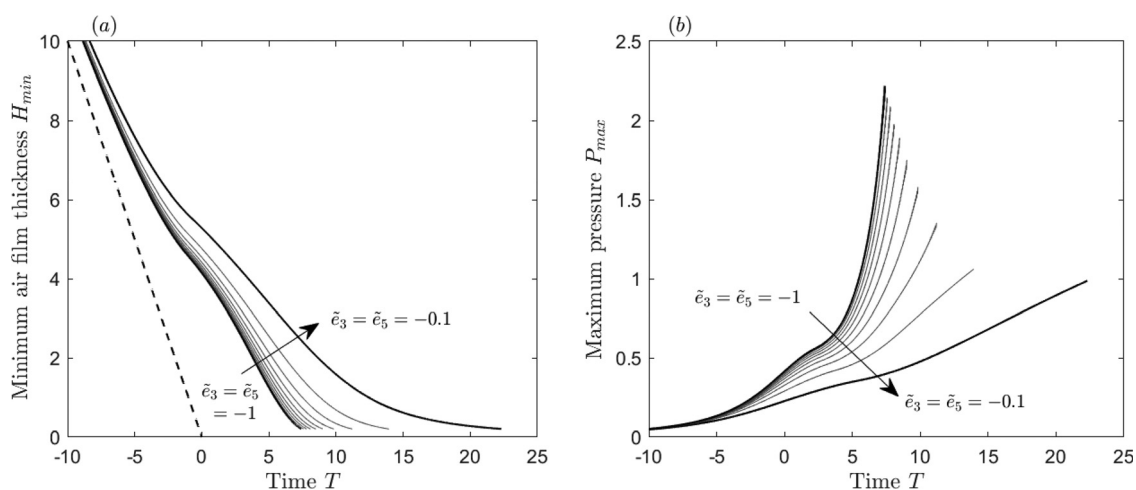


**FIG. 5.** The (a) minimum air film thickness and the (b) maximum pressure as a function of time $T$ for viscoelastic surfaces with coefficients $\tilde{e}_3 = \tilde{e}_5$ ranging from $-1$ to $-0.1$ in intervals of 0.1. The dashed line in figure (a) corresponds to the minimum film thickness in the absence of air cushioning.
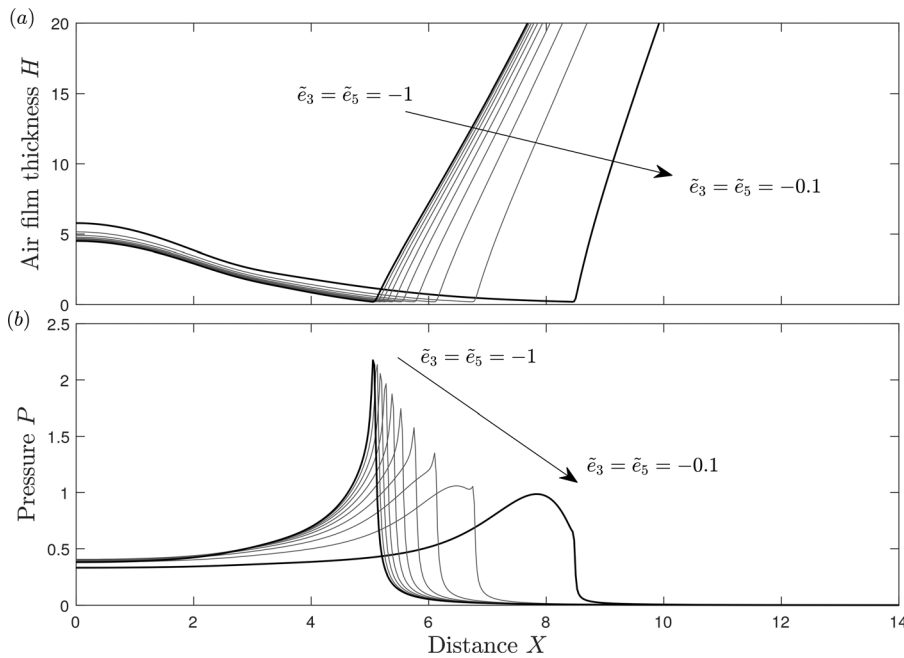
**FIG. 6.** As in Fig. 5, except showing (a) the air film thickness $H = F - G$ and (b) the pressure near touchdown.

model leads to an increase in the area of air entrapped at impact. The framework of our model is in two dimensions, and it is realized that droplet impact is clearly a three dimensional phenomenon. Despite this, we are able to use our model to make a qualitative assessment of the size of entrapped air for variations in the surface stiffness and (viscous) damping.

The X-wise symmetry of the solutions allows us to calculate the dimensionless area of entrapped air $B$ as

$$B = 2 \int_0^{X_d} H(X, T_d) \mathrm{d}X, \qquad (30)$$

where $X_d$ is the positive $X$ station of minimum air film thickness and $T_d$ is the touchdown time. It should be stressed that, numerically, touchdown where $H = 0$ is never quite realized due to the parabolic degeneracy of the lubrication equation (22). Therefore, the time of touchdown has to be pre-determined as a point when the air film thickness reduces to a very small positive value. Numerically, the smaller the grid size and time step in the numerical scheme, the smaller we can make this value. However, this has to be balanced with the increased computational cost due to the huge amount of simulations needed to be run to build a parametric picture. In the present section, we therefore set this pre-determined value of air film thickness, where the droplet is considered to have reached touchdown, as $H_{min} = 0.1$ (the solutions in Figs. 4 and 6 are plotted up until $H_{min} = 0.2$, for comparison).

Figure 7 shows how the dimensionless area of entrapped air $B$ depends on the surface parameters $\tilde{e}_3$ and $\tilde{e}_5$, for the viscoelastic surface model. Clearly, for any decrease in magnitude of $\tilde{e}_3$ or $\tilde{e}_5$ there is an increase in the area of entrapped air. The dimensional entrapped air area $b^*$ can be related to the dimensional area $B$ by applying the vertical and horizontal length scales, which yields

$$b^* = \varepsilon^3 R^2 B = \frac{\mu_g R}{\rho_l V} B, \qquad (31)$$

where the pre-factor $B$ is, in the viscoelastic model, a function of the parameters $\tilde{e}_3$ and $\tilde{e}_5$ and its dependency is shown in Fig. 7 for parameters in the range $[-10, -0.1]$. For parameter values of magnitude lower than 0.1, the area of entrapped air continues to increase and for parameters of magnitude higher than 10 the behavior of the droplet is identical to that of a flat rigid surface.
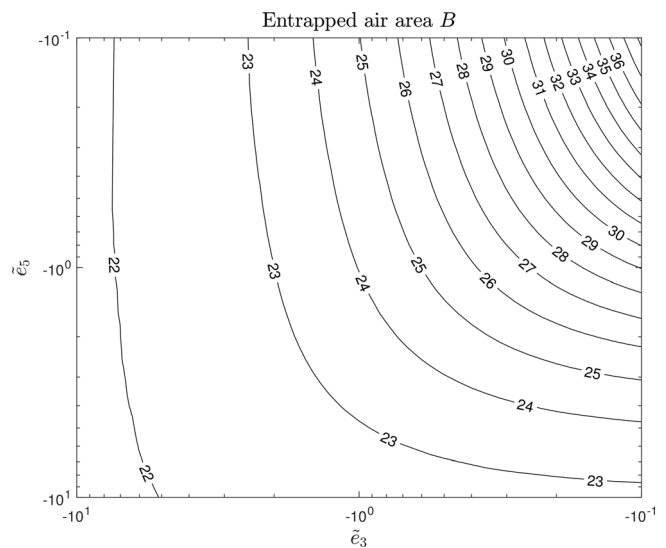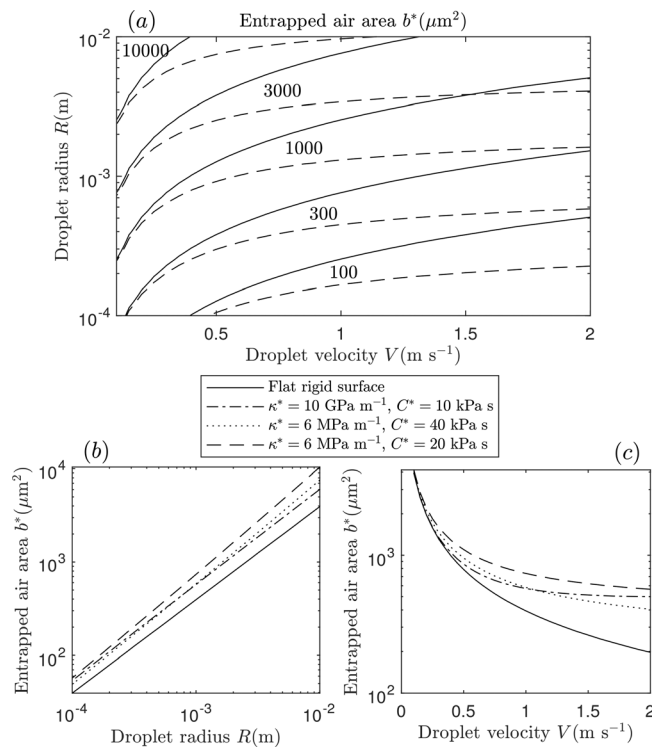


**FIG. 7.** Parametric plot of the entrapped air area $B$ for variations in the parameters $\tilde{e}_3$ and $\tilde{e}_5$ in the viscoelastic model.

Equation (31) for the dimensional entrapped air area highlights the importance of the droplet velocity and radius on the size of entrapped air at impact. For a flat rigid surface, where $B$ is a given constant, droplets with a larger radius will entrap more air due to having a larger free-surface to interact with the air prior to impact and droplets with a larger velocity will entrap less air due to the droplet having less time to deform prior to impact. In the viscoelastic model, the numerical pre-factor $B$ depends on $\tilde{e}_3$ and $\tilde{e}_5$ and formulas for these parameters are given in (25). It is interesting to note that the parameter $\tilde{e}_3$ does not depend on the droplet radius $R$. It is therefore of interest to see how the size of entrapped air varies with droplet velocity and radius for given fluid and structural parameters (the structural parameters of concern here are the stiffness $\kappa^*$ and the damping $C^*$).

Figure 8 gives a comparison produced by results for the dimensional entrapped air area of a water droplet in air over wide ranges of the droplet radius $R$ and velocity $V$, for a flat rigid surface and soft viscoelastic surfaces. We chose to vary the droplet velocity from 0.1 to 2 m s$^{-1}$ and the radius from $10^{-4}$ to $10^{-2}$ m in order to keep the parameter regime mostly contained in the valid model parameter regime given in Fig. 2. Figure 8(a) shows the variations of the entrapped air area $b^*$ as the droplet velocity and radius vary,

comparing a flat rigid surface to a soft viscoelastic surface with spring stiffness $\kappa^* = 6$ MPa m$^{-1}$ and (viscous) damping $C^* = 20$ kPa s. For all combinations of droplet velocity and droplet radius, more air is entrapped by the soft viscoelastic surface, as is to be expected. For small droplet impact velocities, the effect of the soft solid is minimal and it behaves much like a rigid surface. As the droplet velocity increases, the effect of the soft viscoelastic surface is far more profound. From Eq. (31), we can see that for a flat rigid surface the area of entrapped air decreases with increased droplet velocity, whereas for the soft viscoelastic surface, this decrease in entrapped air area is delayed and even halted for increased droplet velocity, for the parameters under consideration here. This can be seen more clearly in Fig. 8(c) where the entrapped air area is given as a function of droplet velocity for a 1 mm water droplet in air, for a variety of spring stiffness $\kappa^*$ and (viscous) damping $C^*$. This is due to higher air film pressures, induced by higher droplet velocities, causing larger surface deformation prior to impact. By considering the shape of the contour lines in Fig. 8(a), variations of the droplet radius have a less profound influence on the increase in entrapped air on a soft viscoelastic solid compared to a flat rigid surface. This is shown more clearly in Fig. 8(b), where the entrapped air area is plotted as a function of droplet radius for an impact velocity of 1 m s$^{-1}$. On a logarithmic scale, the increased amount of entrapped air due to the impact on a soft viscoelastic surface is almost independent of droplet radius.

## IV. IMPACT ON A FLEXIBLE SURFACE

We now turn our attention to analyzing the air cushioning effect in droplet impact on a more general flexible surface, where all terms except for the damping term in Eq. (24) are retained. The model here is an elastic plate, or membrane, sitting atop a bed of springs, which is akin to many previous studies on fluid-flexible surface interactions.[46–52] The depth of the bed of springs is assumed to be much larger than $O(\varepsilon^2 R)$, and so the influence of the rigid base on which the springs are based can be ignored. Thus, this rather general model is a semi-infinite flexible surface which includes all relevant physics in two-dimensional deformation. This case is similar to Sec. III; however, now the influence of the elastic plate is considered and so physical parameters to account for surface rigidity, tension, and inertia are now also included and examined. A schematic of the problem setup is given in Fig. 9.

In practice, the magnitude of the dimensionless parameters $\tilde{e}_i$ can vary dramatically and over a number of orders of magnitude. By considering Fig. 2, we can see the range of droplet velocities and radii where our model is applicable, and it is the structural parameters that will require special attention. Explicit formulas for the parameters $\tilde{e}_i$ are given in (25) and if we consider a water droplet of radius 1 mm and impact velocity 1 m s$^{-1}$, we are able to obtain an order of magnitude estimate of the dimensionless parameters $\tilde{e}_i$ in terms of their corresponding structural coefficient,

$$(|\tilde{e}_1|, |\tilde{e}_2|, |\tilde{e}_3|, |\tilde{e}_4|) \sim (10^7 B^*, 10^{-2} T_t^*, 10^{-11} \kappa^*, 10^1 M^*). \quad (32)$$

Therefore, if we wish for the dimensionless surface parameters $\tilde{e}_i$ to be of order one, plus or minus a few orders of magnitude, then we now know what order of magnitude the dimensional structural parameters need to be in our model. If we wish to consider the rather large range of parameter magnitudes $10^{-4} < |\tilde{e}_i| < 10^4$, then this implies our structural parameters are of the
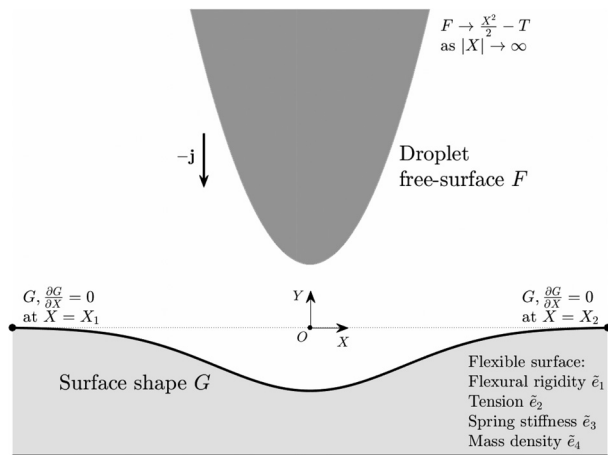


**FIG. 8.** For the impact of a water droplet in air, (a) variations in the entrapped air area $b^*(\mu m^2)$ as the droplet velocity $V$(m s$^{-1}$) and radius $R$(m) vary for a flat rigid surface (solid line) and a soft viscoelastic surface with spring stiffness $\kappa^* = 6$ MPa m$^{-1}$ and (viscous) damping $C^* = 20$ kPa s (dashed line), (b) entrapped air area for a droplet velocity of 1 m s$^{-1}$ and variations in droplet radius, and (c) entrapped air area for a droplet of radius 1 mm and variations in droplet velocity. In figures (b) and (c), the results are presented for a variety of spring stiffness $\kappa^*$ and (viscous) damping $C^*$.

**FIG. 9.** Schematic representation of the scaled, non-dimensional problem setup of droplet impact on a flexible surface pre-impact (this is not a solution).

order $10^{-11} < B^* < 10^{-3}$, $10^{-2} < T_t^* < 10^6$, $10^7 < \kappa^* < 10^{15}$, and $10^{-5} < M^* < 10^3$. Rather unsurprisingly, we require a flexural rigidity $B^*$ of small magnitude. The flexural rigidity can be defined by the formula

$$B^* = \frac{Eh^3}{12(1-\nu^2)}, \tag{33}$$

where $E$ is the Young's Modulus of the material, $h$ is the elastic thickness, and $\nu$ is the Poisson ratio. Therefore, for the flexural rigidity $B^*$ to be of a suitably small magnitude, we would require a combination of a relatively low Young's Modulus combined with thin plates. Examples of impacts involving such a combination exist in nature, such as impact on leaves,[3] and for impact on thin foils of certain materials.[54]

The surface shape equation (24) is then solved numerically, again coupled with Eqs. (14) and (22). The boundary conditions and the numerical treatment are slightly different from Sec. III, due to the spatial derivatives now present in the surface equation. Because of the spatial derivatives, boundary conditions for the surface shape $G$ are required now at fixed positions. We choose clamped plate boundary conditions, which are

$$G = \frac{\partial G}{\partial X} = 0 \quad \text{at } G = X_1, X_2, \tag{34}$$

where $X_1$ and $X_2$ are given $X$ stations and will be stated in each case. Typically, we take $X_1$ and $X_2$ as the end points of the computational domain. The same efficient numerical scheme applied in Sec. III cannot practically be used here because of the increased numerical complexity due to sixth order derivatives occurring when substituting the surface equation (24) into the lubrication equation (22). We therefore adopt a more standard approach of iterating between each of Eqs. (14), (22), and (24) and solving for $P$, $F$, and $G$, respectively, until convergence, using the same algorithms outlined in Sec. III.

### A. Free-surface and pressure profile solution

Figure 10 shows the solution profiles for the free-surface $F$ and the pressure $P$ for three different values of the stiffness parameter $\tilde{e}_3$,

with the other surface parameters fixed. In practice, zero stiffness is not possible; hence, while all the other parameters are fixed, $\tilde{e}_3 \to 0^-$ is a limiting scenario (the same applies for the other parameters in Sec. IV B). The dashed line in each plot of Fig. 10(a) corresponds to the solution of the flexible surface shape $G$ as touchdown is approached. The results illustrate the outcomes of variations in the stiffness parameter $\tilde{e}_3$; however, variations in any of the other surface parameters yield qualitatively similar results. The solution in the flat surface case is not shown here for brevity, see Fig. 4 for comparisons.

The aim of this section is to highlight the effect the surface flexibility can have on the pre-impact phase of droplet impact, as opposed to the effect of a soft deformable surface considered in Sec. III. Figure 10 shows that much of the same conclusions can be drawn. First, increased surface flexibility leads to a delay to touchdown. This delay to touchdown acts to further decelerate the droplet free-surface and results in a lower pressure buildup underneath the droplet. The pressure peak amplitude is again lower near touchdown for more flexible surfaces. Figure 11 shows the minimum air film thickness and the maximum pressure as functions of time, where it can be seen that this lower pressure buildup is present for all time. Figure 12 compares the solutions of the air film thickness and the pressure near touchdown, showing clearly the reduced pressure peak and increased air entrapment near touchdown for reductions in the magnitude of the stiffness parameter $\tilde{e}_3$.

The main difference to highlight when comparing air cushioning behavior of droplet impact on a flexible surface to impact on a soft viscoelastic surface is the shape of the pressure profile upon touchdown. Here, in Fig. 10, reductions in the magnitude of the parameter $\tilde{e}_3$ lead to reductions in the amplitude of the pressure peak near touchdown, but the peak remains sharp. This is unlike the finding for the viscoelastic surface, where increased deformability leads to a decrease in the pressure peak amplitude and also a rounder, softer peak. This could be due, in part, to the more abrupt approach to touchdown seen in Fig. 11, for a flexible surface, compared with the gentler approach seen in Fig. 5, for a soft viscoelastic surface. Also, the droplet free-surface cusp remains relatively sharp in the flexible surface case as deformability increases, while in the viscoelastic case it becomes rounded, which is likely to play a key role in the shape of the pressure peak. However, as the droplet free-surface becomes sharp, surface tension effects will become significant and would need to be considered here in the flexible surface case. At leading order, the local touchdown behavior here is identical to that described in Smith *et al.*[22]

### B. Entrapped air size

Using Eq. (30), we are again able to make a qualitative assessment of how variations in the surface properties affect the size of entrapped air. Here, we perform a study of how individual variations in the parameters $\tilde{e}_1$, $\tilde{e}_2$, $\tilde{e}_3$, and $\tilde{e}_4$ (with $\tilde{e}_5 = 0$) alter the area of entrapped air at touchdown. The size of the air gap at which the calculation of Eq. (30) is performed is 0.26 for this model, which is the smallest achievable for all compared results and larger than that considered in Sec. III due to the more difficult numerical task.

Figure 13 shows how individual variations in the surface parameters $\tilde{e}_1$, $\tilde{e}_2$, $\tilde{e}_3$, and $\tilde{e}_4$ affect the entrapped air area at touchdown. Logarithmic variations of each parameter lead to a similar dependency on the entrapped air area. Each figure exhibits plateauing behavior to the flat rigid surface value for large magnitude parameters and to the
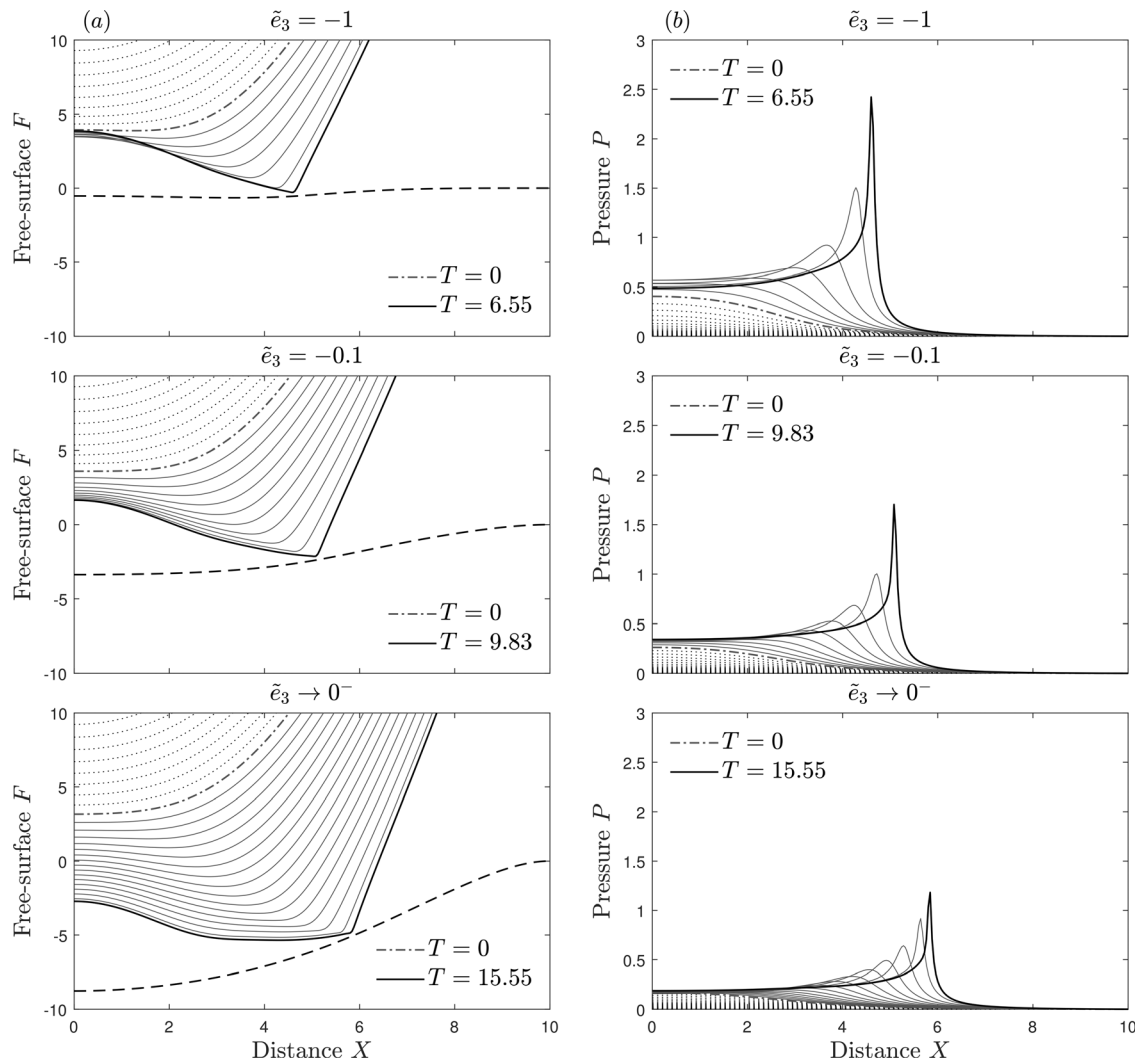
**FIG. 10.** Solution profiles, showing the evolution of (a) the free-surface height $F$ and (b) the pressure $P$ for normal impact of a droplet onto a flexible surface with parameters $(\tilde{e}_1, \tilde{e}_2, \tilde{e}_3, \tilde{e}_4, \tilde{e}_5) = (-1, 1, \tilde{e}_3, -1, 0)$ and $\tilde{e}_3 = -1$, $\tilde{e}_3 = -0.1$, and $\tilde{e}_3 \to 0^-$. The boundary of the flexible surface is at $[X_1, X_2] = [-10, 10]$. The solutions are shown in integer time increments except for the final thick solid line, which is the solution just prior to touchdown, and the dashed line, which is the flexible surface solution $G$ just prior to touchdown. The dashed-dotted line is the solution at $T = 0$ where the droplet would touchdown on an undisturbed surface in the absence of air cushioning.

value for the solution as the parameter tends to zero, except for Fig. 13(d), where, in the current setting, variations of the magnitude of the mass density parameter $\tilde{e}_4$ much lower than 1 lead to an unbounded surface velocity $\partial G/\partial T$ at some point. From Fig. 13, it is clear that any increase in the flexibility of the surface leads to an increase in entrapped air.

## V. CONNECTION WITH EXPERIMENTS

In Secs. III and IV, we performed a numerical study into the air cushioning phase of droplet impact on the deformable surfaces. Here, we now attempt to make connections to recent experiments. Due to our work being two dimensional and approximate, using a number of assumptions on the fluid and structural parameters, these connections are tentative, but they seem encouraging nonetheless.

### A. Entrapped air

In Langley *et al.*[8] it was found, experimentally, that droplet impacts onto softer, more deformable, solids would entrap more air. They performed experiments using ultra-high-speed interferometry to capture the droplet free-surface at impact, and varied the droplet velocity and the surface stiffness. We have qualitative agreement with these findings in our analytical results. We found in Secs. III and IV that reductions in surface stiffness resulted in an increase in entrapped air. A more subtle point to make from our analytical work is the non-intuitive dependency of the size of entrapped air on the droplet velocity. On a rigid flat surface, the size of entrapped air will decrease for higher velocities, whereas for impact on a soft viscoelastic surface this reduction is delayed and even halted for increased impact velocities. This is alluded to in Langley *et al.*[8] also and, although described in terms of gas compression while our
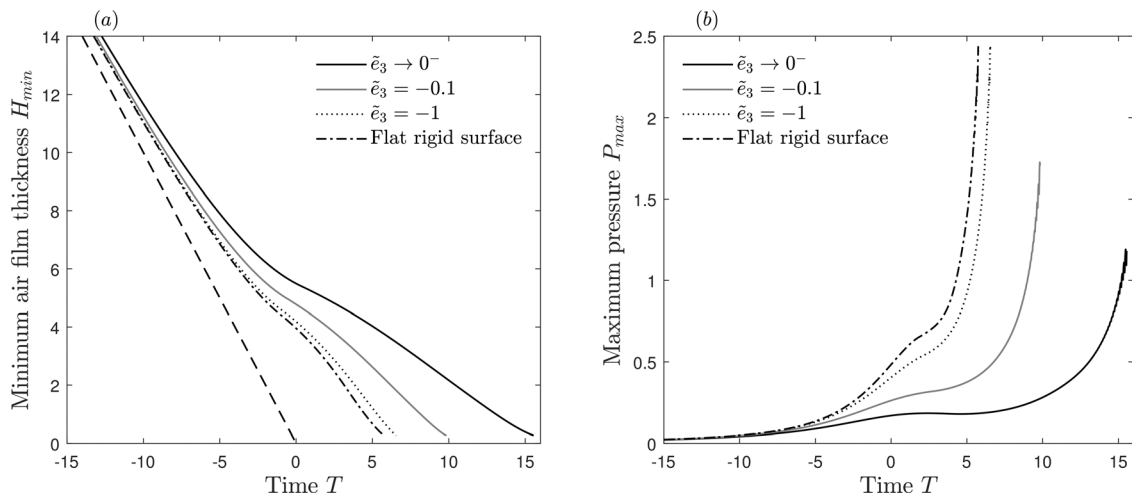
**FIG. 11.** The (a) minimum air film thickness and the (b) maximum pressure as a function of time $T$ for a flat rigid surface and flexible surfaces with coefficients $(\tilde{e}_1, \tilde{e}_2, \tilde{e}_3, \tilde{e}_4, \tilde{e}_5) = (-1, 1, \tilde{e}_3, -1, 0)$, a range of values of $\tilde{e}_3$ and boundary $[X_1, X_2] = [-10, 10]$. In (a), the dashed line corresponds to the solution in the absence of air cushioning.

work is incompressible, they show that entrapped air can increase with increased droplet velocity for impact on the soft solids. The increase in entrapped air on more deformable surfaces is also likely to influence the overall outcome of the droplet impact, with implications on rebounding[9,20,21] and splashing[31] droplets.

## B. Implications on splashing

Howland *et al.*[12] focused their study on how soft deformable surfaces affect droplet splashing. They performed experiments by impacting ethanol droplets on silicone or acrylic substrates of varying stiffnesses, and found that the lower the stiffness, the less likely the droplet was to splash. This was found to be most likely due to higher stiffness substrate having sheet ejection of higher velocity, resulting in the sheet leaving the surface and breaking up, forming a corona splash. By contrast, for less stiff surfaces, the ejected sheet is of lower velocity and does initially leave the substrate, but can fall back down onto the substrate and slow down, suppressing the splash. They were unable to investigate the sheet ejection experimentally, because of the small time
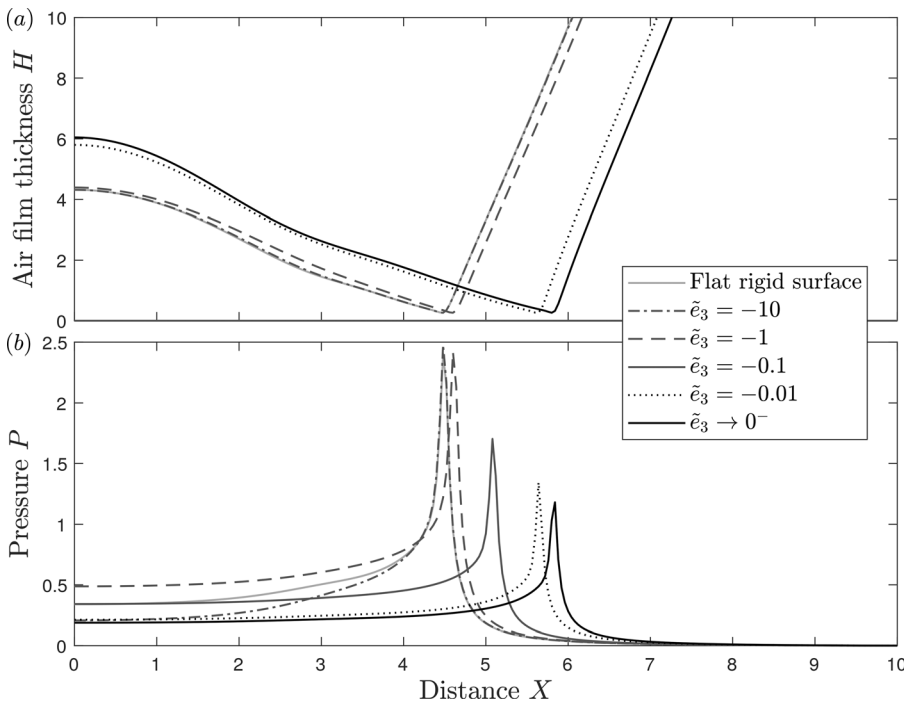


**FIG. 12.** As in Fig. 11, except showing (a) air film thickness $H$ and (b) pressure $P$ near touchdown.
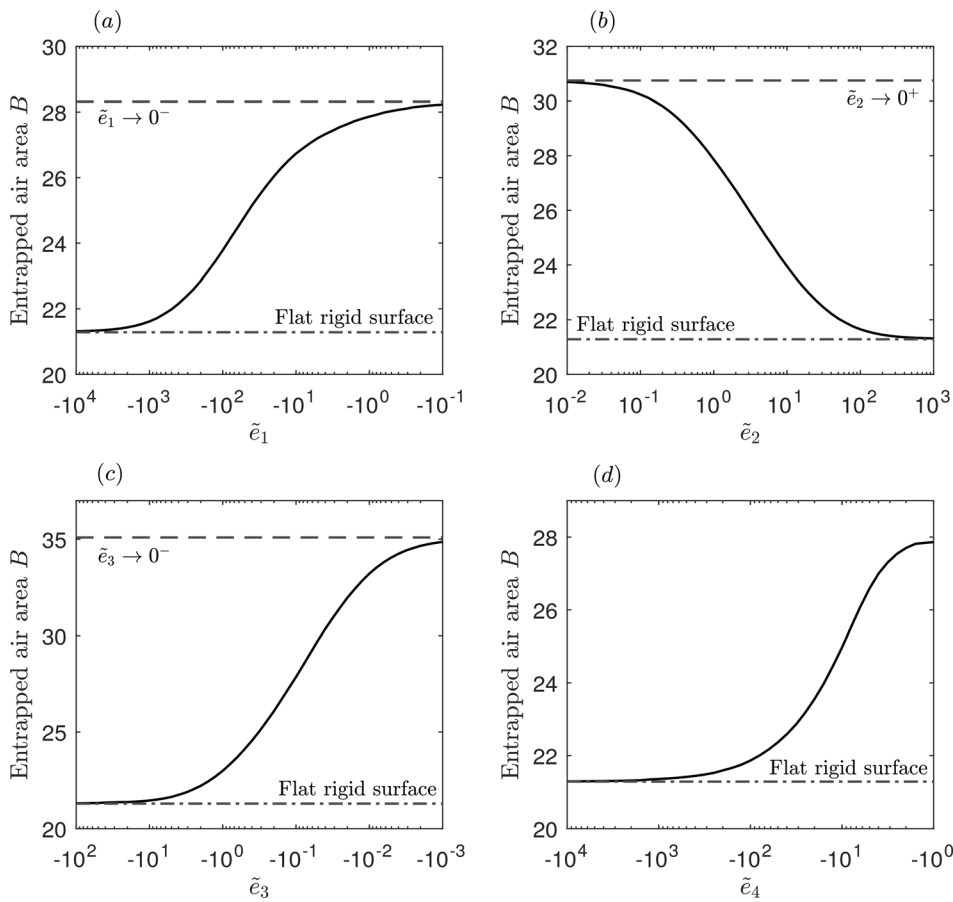
**FIG. 13.** Area of entrapped air $B$ for droplet impact on the flexible surfaces, with a boundary of $[X_1, X_2] = [-10, 10]$ and surface parameters (a) $(\tilde{e}_1, \tilde{e}_2, \tilde{e}_3, \tilde{e}_4, \tilde{e}_5) = (\tilde{e}_1, 1, -0.1, -1, 0)$ for variations in $\tilde{e}_1$, (b) $(-1, \tilde{e}_2, -0.1, -1, 0)$ for variations in $\tilde{e}_2$, (c) $(-1, 1, \tilde{e}_3, -1, 0)$ for variations in $\tilde{e}_3$ and (d) $(-1, 1, -0.1, \tilde{e}_4, 0)$ for variations in $\tilde{e}_4$. In each figure, the dashed-dotted line corresponds to the value for a flat rigid surface and the dashed line corresponds to the limiting value as the relevant parameter tends to zero. In (d), the limit as the mass density parameter $\tilde{e}_4$ tends to zero cannot be found, due to an unbounded surface velocity.

and length scales associated with it. Hence, they investigated it using numerical simulation, and found that lowering the surface stiffness reduced the contact pressure just before the sheet is ejected. Our results in Secs. III and IV show clearly that reducing the surface stiffness leads to a reduction in the pressure peak just prior to impact. In particular, the results in Sec. III for droplet impact on a viscoelastic solid show a softening of the pressure peak prior to touchdown. Although our study is solely focused on pre-impact behavior, this reduction in pressure appears important in understanding the reduced sheet ejection speed mentioned in Howland et al.,[12] which results in potential splash suppression.

## VI. LARGE SURFACE DEFORMATION

In this section, we examine the effect of large surface deformations on the system. Here, we will consider the system in the limit $\tilde{e}_1 \to 0$, $\tilde{e}_2 \to 0$, $\tilde{e}_3 \to 0$, and $\tilde{e}_5 \to 0$, where Eq. (24) may be written simply as $\tilde{e}_4 \partial^2 G / \partial T^2 = P$. What this allows us to do is reduce our previous system of three equations to two, by writing $H = F - G$, the air film thickness. The new system is now

$$\frac{\partial^2 H}{\partial T^2} = \frac{1}{\pi}(\text{PV})\int_{-\infty}^{\infty} \frac{\partial P}{\partial \zeta}(\zeta, T)\frac{d\zeta}{X - \zeta} - \frac{P}{\tilde{e}_4}, \quad (35a)$$

$$\frac{\partial}{\partial X}\left(H^3\frac{\partial P}{\partial X}\right) = 12\frac{\partial H}{\partial T}. \quad (35b)$$

Equations (35a) and (35b) can be further simplified by rescaling all the variables to account for $|\tilde{e}_4|$. We are interested in the case of $\tilde{e}_4$ being small (and negative) and the timescale being large, as for large surface deformations we expect touchdown to be further delayed. Hence, we take the following rescaling:

$$(H, P, X, T) = (|\tilde{e}_4|^{-1}\bar{H}, |\tilde{e}_4|^2\bar{P}, |\tilde{e}_4|^{-1/2}\bar{X}, |\tilde{e}_4|^{-1}\bar{T}); \quad (36)$$

then Eqs. (35a) and (35b) reduce to, dropping the overbar notation,

$$\frac{\partial^2 H}{\partial T^2} = P, \quad (37a)$$

$$\frac{\partial}{\partial X}\left(H^3\frac{\partial P}{\partial X}\right) = 12\frac{\partial H}{\partial T}, \quad (37b)$$

where the relative error in ignoring the Cauchy integral is $O(|\tilde{e}_4|^{3/2})$, which is suitably small. We impose

$$H \sim \frac{X^2}{2} - T, \quad P \sim 0, \quad \text{as } |X| \to \infty \quad \text{or} \quad T \to -\infty, \quad (38)$$

as the far-field conditions.

As was first remarked in Korobkin et al.[59] for a different model, the pressure-shape law (37a) can be viewed as an alternative to the Cauchy–Hilbert law in Smith et al.,[22] such as in pressure-displacement laws in interacting boundary layers.[60,61] The new coupled system (37) allows us to make far more analytical progress than for the previous system examined computationally in Secs. III and IV.

### A. Computational solutions

The coupled system (37) was solved numerically using a scheme identical to that outlined in Sec. III, with the new local pressure-shape relationship (37a). As is to be expected, this scheme is far faster than the one involving the Cauchy–Hilbert integral. An appropriate spatial domain here was found to be $[-20, 20]$.

Figure 14 shows the time-marched solutions of $H$ and $P$. The mechanisms are essentially the same as before. The droplet is released at some suitably large negative time and begins to approach the surface. The air film thickness is initially parabolic and as the air film thickness begins to decrease, the pressure begins to rise in a single peak and results in the air film thickness deviating from the parabolic shape. The pressure then starts to have two peaks as the air film thickness approaches zero in two different locations equidistant from the centerline.

The solutions of $H$ and $P$ in Fig. 14 show clearly two traits of droplet impact on a very deformable surface that can be intuitively expected from the results in Secs. III and IV. Figure 14 shows solutions up until $T = 60$. The longer time scales associated here are clear to see and it is expected that touchdown is not reached in finite time. We can also see that the horizontal bubble extent has significantly increased.

### B. Large time behavior

The computational results given in Fig. 14 show that the time scales involved in this system are large and suggest that perhaps touchdown in finite time is not reached on this timescale. Hence, we seek a solution at large positive time. Suppose that the scaled air thickness and pressure are rising relatively fast in spatial terms, near a region

where $X = cT^\alpha$ say, with $\alpha$ a positive constant. The length scaling in this region then takes the form

$$X = cT^\alpha + T^m \xi \quad \text{as } T \to \infty, \tag{39}$$

where $\xi$ is order unity, the constants $\alpha$ and $m$ are unknown, and in order for the region to be local, we require that $m < \alpha$. Expansions of $H$ and $P$ are then taken in the rather general form

$$H \sim T^\lambda \hat{H}(\xi), \tag{40a}$$

$$P \sim T^{\lambda+2\alpha-2m-2} \hat{P}(\xi), \tag{40b}$$

where $\lambda$ is an unknown constant. It is to be expected that $\lambda \leq 0$ as $H$ is not growing in time, and the expansion of $P$ is inferred from seeking a balance in Eq. (37a). Substitution of the expansions (40) into the governing equations (37a) and (37b) leads to the system

$$\alpha^2 c^2 \frac{d^2 \hat{H}}{d\xi^2} = \hat{P}, \tag{41a}$$

$$\frac{d}{d\xi}\left(\hat{H}^3 \frac{d\hat{P}}{d\xi}\right) = -12\alpha c \frac{d\hat{H}}{d\xi}, \tag{41b}$$

to the leading order, subject to

$$m = \lambda + \frac{\alpha - 1}{3}, \tag{42}$$

and also $3\lambda < 2\alpha + 1$. The system (41) can be further reduced to an ordinary differential equation in $\hat{H}$ alone

$$\hat{H}^3 \frac{d^3 \hat{H}}{d\xi^3} = -\frac{12}{\alpha c}\hat{H} + k, \tag{43}$$

where $k$ is an integration constant and must be positive in order to keep $\hat{H}$ positive. Equations of the form (43) occur commonly in a number of applied mathematics problems[26,62,63] and it is expected that the solution $\hat{H}$ will tend to a non-zero constant $\alpha c k / 12$ as $\xi \to -\infty$. Perturbations to this constant value occur, such that
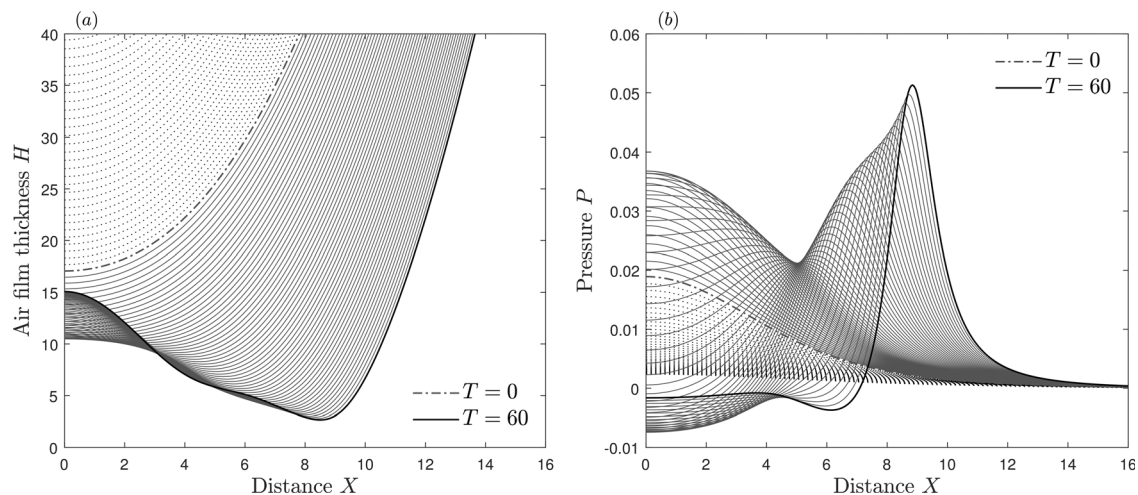


**FIG. 14.** Solution profiles of the (a) air film thickness $H$ and (b) pressure $P$. The solutions are shown in integer time increments up until $T = 60$.

$$\hat{H} \sim \frac{\alpha c k}{12} + \Re[\gamma_1 \exp{(\gamma_2 \xi)}] \quad \text{as } \xi \to -\infty, \tag{44}$$

where $\Re$ denotes the real part and $\gamma_1$ and $\gamma_2$ are complex constants. Note, if we were to take the perturbation in the form $\gamma_1 \exp{(\gamma_2 \xi)}$, where $\gamma_1$ and $\gamma_2$ are real constants, then that would lead to $\gamma_2 < 0$ and thus an exponentially growing perturbation. The complex constant $\gamma_2$ satisfies $\gamma_2^3 = -q$, where $q = (12/\alpha c k^{3/4})^4$, and the complex constant $\gamma_1$ remains arbitrary. There are then three possible solutions for $\gamma_2$, and we wish to choose the ones such that $\Re[\gamma_2] > 0$ so that we have a decaying perturbation. There are two such solutions, $\gamma_2 = q^{1/3}(1 \pm i\sqrt{3})/2$, which leads to the large negative $\xi$ asymptote taking the form

$$\hat{H} \sim \frac{\alpha c k}{12} + \exp{\left(\frac{1}{2}q^{1/3}\xi\right)} \left\{ \gamma_{1,1} \cos{\left(\frac{\sqrt{3}}{2}q^{1/3}\xi\right)} \right.$$
$$\left. + \gamma_{1,2} \sin{\left(\frac{\sqrt{3}}{2}q^{1/3}\xi\right)} \right\} \quad \text{as } \xi \to -\infty, \tag{45}$$

where $\gamma_{1,1}$ and $\gamma_{1,2}$ remain arbitrary, still. For large positive $\xi$, it can be readily shown that

$$\hat{H} \sim \lambda_1 \xi (3\ln\xi)^{1/3} \quad \text{as } \xi \to \infty, \tag{46}$$

where $\lambda_1 = (12/\alpha c)^{1/3}$. From Eq. (41a), we can also show that the corresponding $\hat{P}$ asymptote is

$$\hat{P} \sim \lambda_2 \xi^{-1}(3\ln\xi)^{-2/3} \quad \text{as } \xi \to \infty, \tag{47}$$

where $\lambda_2 = \alpha^2 c^2 \lambda_1$.

Equation (43) was then solved numerically as a boundary value problem using Newton–Raphson iterations, with the asymptotes for $\hat{H}$ (45) and (46) imposed at suitable large negative and positive $\xi$ values, respectively. The corresponding solution for $\hat{P}$ is then calculated from Eq. (41a) using central finite differences. Without loss of generality, the constants $\alpha^2 c^2$, $12/(\alpha c)$ and $k$ can be normalized to unity by a division of $\hat{H}$, $\xi$, $\hat{P}$ by $\alpha c k/12$, $(\alpha c/12)^{4/3}k$, $(12^5\alpha c)^{1/3}/k$ in turn. Figure 15 shows the solution of $\hat{H}$ and $\hat{P}$ for $\gamma_{1,1} = \gamma_{1,2} = 1$.
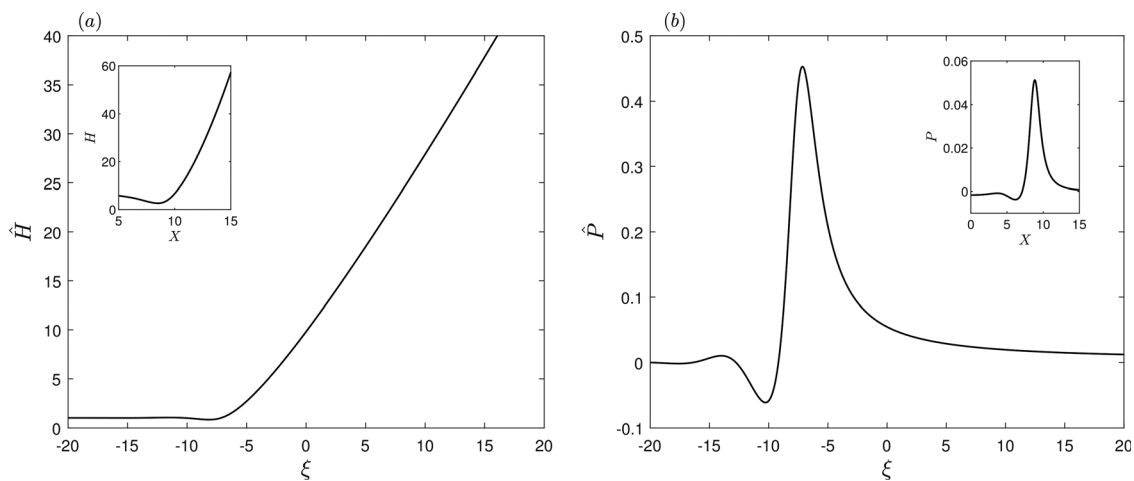
Variations in the value, even sign, of the parameters $\gamma_{1,1}$ and $\gamma_{1,2}$ yield identical results to that presented in Fig. 15.

The solutions given in Fig. 15 show excellent agreement locally with the solutions of the full system (37), solved numerically and presented in Fig. 14, at large time, especially the solution found for $\hat{P}$ which is qualitatively identical to the solution of $P$ at large times (the large time solution to the full system is shown in the inset of Fig. 15, for comparison).

Now, let us move further rightwards into positive $\xi$ by considering $\xi = \mathscr{D}\bar{X}$, where $\mathscr{D} \gg 1$ and $\bar{X}$ is of order unity. We can infer expansions of $\hat{H}$ and $\hat{P}$ from their large positive $\xi$ asymptotes (46) and (47),

$$\hat{H} = \mathscr{D}(\hat{H}_0(3\ln\mathscr{D})^{1/3} + \hat{H}_1(3\ln\mathscr{D})^{-2/3} + \cdots), \tag{48a}$$

$$\hat{P} = \mathscr{D}^{-1}(\hat{P}_0(3\ln\mathscr{D})^{-2/3} + \hat{P}_1(3\ln\mathscr{D})^{-5/3} + \cdots). \tag{48b}$$

To leading order, Eq. (43) then yields $\mathrm{d}^3\hat{H}_0/\mathrm{d}\bar{X}^3 = 0$ and matching requires $\hat{H}_0 \sim \lambda_1 \bar{X}$ as $\bar{X} \to 0^+$. Hence

$$\hat{H}_0 = \lambda_1\bar{X} + \mu_1\bar{X}^2, \tag{49}$$

where $\mu_1$ is a positive constant. Now we can see that, at the leading order for both $\hat{H}$ and $\hat{P}$,

$$\hat{H} \sim \mu_1\bar{X}^2, \quad \hat{P} \sim 0 \quad \text{as } \bar{X} \to \infty, \tag{50}$$

which is a form resembling the far-field condition (38). In light of (39), (40a) and (50), $H$ emerges as

$$H \sim \mu_1 \mathscr{D}^{-2} T^{2(1-\alpha)/3-\lambda}(X - cT^\alpha)^2, \tag{51}$$

just to the right of the local zone, which, as far as the $X^2$ requirement in (38) is concerned, indicates that the constants must satisfy

$$\alpha = 1 - \frac{3\lambda}{2}, \tag{52a}$$

$$m = \frac{\lambda}{2}; \tag{52b}$$



**FIG. 15.** Solution of equation (a) (43) for $\hat{H}$, and then (b) (41a) for $\hat{P}$, given $\hat{H}$, in normalized form for $\gamma_{1,1} = \gamma_{1,2} = 1$. The *inset* of both figures shows the corresponding local solution of the full system (37) at $T = 60$ for (a) $H$ and (b) $P$.

hence, any $\lambda \leq 0$ works here. To the right of the above local region, we have the balance $H_{TT} \sim 0$, which when matching to (38) at infinity gives the solution

$$H \sim \frac{X^2}{2} - T, \qquad (53)$$

which in turn matches with the far-field solution.

The most acceptable looking solution to arise from this analysis would be if $\lambda = 0$, resulting in $\alpha = 1$ and $m = 0$, with $\xi = X - cT$ and $H$ and $P$ depending on $\xi$ alone. This nonlinear traveling wave form is described fully by (39)–(53), capturing the large time features of the full system (37) successfully and confirming the absence of touchdown on this timescale.

The analysis here is a similar one to that seen in Purvis and Smith[26] and is analogous to a finite-time breakup formulation.[22,64] A physical interpretation of this large time analysis of the large surface deformation system could well be the increased gliding extent observed in Langley et al.[8] for droplet impacts onto soft solids. Gliding occurs when the droplet does not make contact with the substrate at the kink of the dimple, and instead glides on a thin air layer. In Langley et al.,[8] this is seen to occur more frequently and to a greater extent for more deformable surfaces. This could be interpreted as what is occurring in the numerical results for the reduced system in Fig. 14, with the increased time scales and horizontal extent of the kink being potential traits of droplet gliding in the absence of defects and localized wetting.[65]

## VII. CONCLUSIONS

A fluid–structure interaction model describing the pre-impact air cushioning behavior of a droplet impacting a deformable surface has been developed. It rationally couples the thin film lubrication flow of the air to an approaching quasi-inviscid droplet approaching from above and a membrane-type model of the deformable surface below. Building on previous work by Smith et al.,[22] the model assumes a deformable surface deflection of the same order as the droplet free-surface deformation, which allows us to couple the surface deflection with the air film pressure and free-surface deflection.

The deflection of the surface depends on the parameters describing the surface properties, which are incorporated into the membrane type deformable surface equation. These parameters correspond to the surface rigidity, tension, spring stiffness, mass density and damping. We considered two separate major cases of the surface equation. The first, a viscoelastic model, only considered the surface stiffness and the (viscous) damping. Numerical solutions to this system were presented and a number of conclusions were drawn. It was found that by lowering the magnitude of the surface parameters and increasing deformability, the approach to touchdown is considerably delayed, pressure buildup is decreased and more air is entrapped as touchdown is approached. For sufficiently low magnitude parameters, the pressure peak as touchdown is approached is a round one, as opposed to a sharp peak seen before on a rigid surface. The pressure peak is also seen to be located just behind the advancing cusp of the air film thickness, resulting in an increased extent of the air film as touchdown is approached. A numerical analysis was also conducted on the effect of variations of droplet radius and impact velocity on the size of entrapped air at impact, comparing a flat rigid surface to soft viscoelastic surfaces. It was found that the increase in entrapped air due to a

soft viscoelastic surface was almost independent of droplet radius, on a logarithmic scale, while it is strongly dependent on the droplet velocity. For a flat rigid surface, increased droplet velocity results in decreased air entrapment, while for an impact on a soft solid, this decrease in air entrapment is delayed and even halted for increased droplet velocity. A more general, flexible surface was then considered and broadly the same conclusions can be drawn here as for the viscoelastic surface case. A substantial difference, however, is that for a flexible surface, the pressure peak as touchdown is approached remains sharp, despite reductions in amplitude, for increased flexibility. It is shown that reductions in magnitude of each parameter corresponding to the flexural rigidity, tension, stiffness and mass density (for an undamped flexible surface) resulted in an increased air entrapment. Qualitative connections of these findings were made to recent experimental work by Howland et al.[12] and Langley et al.[8]

A case was then considered where we sought a solution in the limit of large surface deformations, for which the air film thickness is dominated by the surface deformation rather than by the free-surface deformation. This leads to a new system of governing equations which is similar to that of the flat rigid surface impact, albeit with a new pressure-shape relationship. This new system, solved computationally, showed the results highlighting the significant increase in horizontal bubble extent and delay to touchdown. A large time analysis was found to give excellent agreement with the full numerical results and confirmed the apparent absence of touchdown (thus hinting at so-called gliding) for that particular system.

The results presented in this paper have broad and important implications. Reductions in the pressure peaks forming underneath the droplet are important when considering impact led damage and ensuing, post-impact dynamics. For example, rain droplet impact on wind turbines can, over time, lead to significant erosion of the wind turbine blades.[66] Reduced pressure peaks appear to also be significant in reducing splashing,[12] which, in turn, has a number of vital implications, such as in aircraft safety,[1,67] pesticide application,[68] forensic science,[69] and many others. Our results should also help engineer novel non-wetting and protective surfaces where impact pressure plays an important role. Our results also point toward a consequence of increased air entrapment, which is undesirable in inkjet printing applications,[2] for example.

While the present study focuses solely on the pre-impact dynamics of droplet impact on the deformable surfaces, important questions remain about what happens next; post-impact. The problem of droplet post-impact theory onto deformable surfaces has been tackled previously[13,15] by ignoring the air cushioning phase and the entrapped air. However, these features do influence the post-impact dynamics,[26,70] and so questions remain on how this occurs in impact on deformable surfaces. One possible alternative to the air cushioning model presented here and the classic Wagner model of impact theory would be to use direct numerical simulation to analyze how air cushioning effects influence post-impact dynamics. While progress has been made considering a flat surface,[31] accurately modeling a deformable surface in such a simulation has not been achieved yet to the best of our knowledge.

The authors have no conflicts to disclose.

## DATA AVAILABILITY

The data that support the findings of this study are available from the corresponding author upon reasonable request.

## REFERENCES

[1]L. Wang, Q. Gong, S. Zhan, L. Jiang, and Y. Zheng, "Robust anti-icing performance of a flexible superhydrophobic surface," Adv. Mater. **28**, 7729–7735 (2016).

[2]D. B. van Dam and C. L. Clerc, "Experimental study of the impact of an ink-jet printed droplet on a solid substrate," Phys. Fluids **16**(9), 3403–3414 (2004).

[3]T. Gilet and L. Bourouiba, "Fluid fragmentation shapes rain-induced foliar disease transmission," J. R. Soc., Interface **12**, 20141092 (2015).

[4]T. Maitra, C. Antonini, M. K. Tiwari, A. Mularczyk, Z. Imeri, P. Schoch, and D. Poulikakos, "Supercooled water drops impacting superhydrophobic textures," Langmuir **30**(36), 10855–10861 (2014).

[5]T. Maitra, M. K. Tiwari, C. Antonini, P. Schock, S. Jung, P. Eberle, and D. Poulikakos, "On the nanoengineering of superhydrophobic and impalement resistant surface textures below the freezing temperature," Nano Lett. **14**, 172–182 (2014).

[6]J. Hao, "Effect of surface roughness on droplet splashing," Phys. Fluids **29**, 122105 (2017).

[7]C. Liu, Q. Liu, and Z. Lin, "Dynamical behavior of droplets transiently impacting on superhydrophobic microstructures," Phys. Fluids **32**, 103304 (2020).

[8]K. R. Langley, A. A. Castrejon-Pita, and S. T. Thoroddsen, "Droplet impacts onto soft solids entrap more air," Soft Matter **16**, 5702–5710 (2020).

[9]S. Mitra, Q. Vo, and T. Tran, "Bouncing-to-wetting transition of water droplets impacting soft solids," Soft Matter **17**, 5969–5977 (2021).

[10]P. B. Weisensee, J. Tian, N. Miljkovic, and W. P. King, "Water droplet impact on elastic superhydrophobic surfaces," Sci. Rep. **6**, 30328 (2016).

[11]T. Vasileiou, J. Gerber, J. Prautzsch, T. M. Schutzius, and D. Poulikakos, "Superhydrophobicity enhancement through substrate flexibility," Proc. Natl. Acad. Sci. U. S. A. **113**, 13307–13312 (2016).

[12]C. J. Howland, A. Antkowiak, J. R. Castrejon-Pita, S. D. Howison, J. M. Oliver, R. W. Style, and A. A. Castrejon-Pita, "It's harder to splash on soft solids," Phys. Rev. Lett. **117**, 184502 (2016).

[13]M. Pegg, R. Purvis, and A. Korobkin, "Droplet impact onto an elastic plate: A new mechanism for splashing," J. Fluid Mech. **839**, 561–593 (2018).

[14]Y. Xiong, H. Huang, and X.-Y. Lu, "Numerical study of droplet impact on a flexible substrate," Phys. Rev. E **101**, 053107 (2020).

[15]M. J. Negus, M. R. Moore, J. M. Oliver, and R. Cimpeanu, "Droplet impact onto a spring-supported plate: Analysis and simulations," J. Eng. Math. **128**, 3 (2021).

[16]S. Poulain and A. Carlson, "Droplet settling on solids coated with a soft layer," arXiv:2106.06320 (2021).

[17]M. B. Lesser and J. E. Field, "The impact of compressible liquids," Annu. Rev. Fluid Mech. **15**, 97–122 (1983).

[18]J. L. Liow, "Splash formation by spherical drops," J. Fluid Mech. **427**, 73–105 (2001).

[19]S. T. Thoroddsen, T. G. Etoh, K. Takehara, N. Ootsuka, and Y. Hatsuki, "The air bubble entrapped under a drop impacting on a solid surface," J. Fluid Mech. **545**, 203–212 (2005).

[20]L. Chen, J. Wu, Z. Li, and S. Yao, "Evolution of entrapped air under bouncing droplets on viscoelastic surfaces," Colloids Surf., A **384**, 726–732 (2011).

[21]L. Chen, E. Bonaccurso, P. Deng, and H. Zhang, "Droplet impact on soft visco-elastic surfaces," Phys. Rev. E **94**, 063117 (2016).

[22]F. T. Smith, L. Li, and G. X. Wu, "Air cushioning with a lubrication/inviscid balance," J. Fluid Mech. **482**, 291–318 (2003).

[23]P. D. Hicks and R. Purvis, "Air cushioning and bubble entrapment in three-dimensional droplet impacts," J. Fluid Mech. **649**, 135–163 (2010).

[24]P. D. Hicks and R. Purvis, "Air cushioning in droplet impacts with liquid layers and other droplets," Phys. Fluids **23**, 62104 (2011).

[25]P. D. Hicks and R. Purvis, "Gas-cushioned droplet impacts with a thin layer of porous media," J. Eng. Math. **102**, 65–87 (2017).

[26]R. Purvis and F. T. Smith, "Air–water interactions near droplet impact," Eur. J. Appl. Math. **15**, 853–871 (2004).

[27]S. Mandre, M. Mani, and M. P. Brenner, "Precursors to splashing of liquid droplets on a solid surface," Phys. Rev. Lett. **102**, 134502 (2009).

[28]M. Mani, S. Mandre, and M. P. Brenner, "Events before droplet splashing on a solid surface," J. Fluid Mech. **647**, 163–185 (2010).

[29]P. D. Hicks and R. Purvis, "Liquid–solid impacts with compressible gas cushioning," J. Fluid Mech. **735**, 120–149 (2013).

[30]Y. Wang, A. Gratadeix, M. Do-Quang, and G. Amberg, "Events and conditions in droplet impact: A phase field prediction," Int. J. Multiphase Flow **87**, 54–65 (2016).

[31]Z. Jian, C. Josserand, S. Popinet, P. Ray, and S. Zaleski, "Two mechanisms of droplet splashing on a solid substrate," J. Fluid Mech. **835**, 1065–1086 (2018).

[32]F. Yeganehdoust, R. Attarzadeh, I. Karimfazli, and A. Dolatabadi, "A numerical analysis of air entrainment during droplet impact on an immiscible liquid film," Int. J. Multiphase Flow **124**, 103175 (2020).

[33]R. Kumar, R. K. Shukla, A. Kumar, and A. Kumar, "A computational study on air entrapment and its effect on convective heat transfer during droplet impact on a substrate," Int. J. Therm. Sci. **153**, 106363 (2020).

[34]H. Shetabivash and A. Dolatabadi, "Numerical investigation of air mediated droplet bouncing on flat surfaces," AIP Adv. **7**, 095003 (2017).

[35]A. A. Korobkin and T. I. Khabakhpasheva, "Regular wave impact onto an elastic plate," J. Eng. Math. **55**, 127–150 (2006).

[36]T. I. Khabakhpasheva and A. A. Korobkin, "Elastic wedge impact onto a liquid surface: Wagner's solution and approximate models," J. Fluids Struct. **36**, 32–49 (2013).

[37]L. Duchemin and N. Vandenberghe, "Impact dynamics for a floating elastic membrane," J. Fluid Mech. **756**, 544–554 (2014).

[38]T. I. Khabakhpasheva and A. A. Korobkin, "Splashing of liquid droplet on a vibrating substrate," Phys. Fluids **32**, 122109 (2020).

[39]T. Nguyen, H. Takahashi, and I. Shimoyama, "MEMS-based pressure sensor with a superoleophobic membrane for measuring droplet vibration," in *Proceedings of 19th International Conference on Solid-State Sensors, Actuators Microsystems (TRANSDUCERS)* (IEEE, 2017), pp. 1152–1155.

[40]R. E. Pepper, L. Courbin, and H. A. Stone, "Splashing on elastic membranes: The importance of early-time dynamics," Phys. Fluids **20**, 082103 (2008).

[41]T. Vasileiou, T. M. Schutzius, and D. Poulikakos, "Imparting icephobicity with substrate flexibility," Langmuir **33**, 6708–6718 (2017).

[42]J.-H. Kim, J. P. Rothstein, and J. K. Shang, "Dynamics of a flexible superhydrophobic surface during a drop impact," Phys. Fluids **30**, 072102 (2018).

[43]X. Huang, X. Dong, J. Li, and J. Liu, "Droplet impact induced large deflection of a cantilever," Phys. Fluids **31**, 062106 (2019).

[44]G. Upadhyay, V. Kumar, and R. Bhardwaj, "Bouncing droplets on an elastic, superhydrophobic cantilever beam," Phys. Fluids **33**, 042104 (2021).

[45]M. Pegg, "Impact of liquid droplets with deformable surfaces," Ph.D. thesis (University of East Anglia, UK, 2019).

[46]P. W. Carpenter and A. D. Garrad, "The hydrodynamic stability of flow over Kramer-type compliant surfaces. Part 1. Tollmien–Schlichting instabilities," J. Fluid Mech. **155**, 465–510 (1985).

[47]J. P. Alexander, T. L. Kirk, and D. T. Papageorgiou, "Stability of falling liquid films on flexible substrates," J. Fluid Mech. **900**, A40 (2020).

[48]P. W. Carpenter and A. D. Garrad, "The hydrodynamic stability of flow over Kramer-type compliant surfaces. Part 2. Flow-induced surface instabilities," J. Fluid Mech. **170**, 199–232 (1986).

[49]J. S. Gajjar and P. Sibanda, "The hydrodynamic stability of channel flow with compliant boundaries," Theor. Comput. Fluid Dyn. **8**, 105–129 (1996).

[50]C. J. Davies and P. W. Carpenter, "Instabilities in a plane channel flow between compliant walls," J. Fluid Mech. **352**, 205–243 (1997).

[51]L. Pruessner, "Waves on flexible surfaces," Ph.D. thesis (University College London, UK, 2013).

[52]L. Pruessner and F. T. Smith, "Enhanced effects from tiny flexible in-wall blips and shear flow," J. Fluid Mech. **772**, 16–41 (2015).

[53]P. Li, B. Zhang, H. Zhao, L. Zhang, Z. Wang, X. Xu, T. Fu, X. Wang, Y. Hou, Y. Fan, and L. Wang, "Unidirectional droplet transport on the biofabricated butterfly wing," Langmuir **34**, 12482–12487 (2018).

[54]M. Contino, L. Allocca, A. Montanaro, G. Cardone, and M. Zaccara, "Dynamic thermal behavior of a GDI spray impacting on a heated thin foil by phase-averaged infrared thermography," SAE Int. J. Adv. Curr. Pract. Mobility (**2**), 512–519 (2020f).

[55]Y. Tagawa, N. Oudalov, A. E. Ghalbzouri, C. Sun, and D. Lohse, "Needle-free injection into skin and soft matter with highly focused microjets," Lab Chip **13**, 1357–1363 (2013).

[56]R. Andrade, O. Skurtys, and F. Osorio, "Experimental study of drop impacts and spreading on epicarps: Effect of fluid properties," J. Food Eng. **109**, 430–437 (2012).

[57]J.-M. Vanden-Broeck and F. T. Smith, "Surface tension effects on interaction between two fluids near a wall," Q. J. Mech. Appl. Math. **61**, 117–128 (2008).

[58]F. Y. Leong and D.-V. Le, "Droplet dynamics on viscoelastic soft substrate: Toward coalescence control," Phys. Fluids **32**, 062102 (2020).

[59]A. A. Korobkin, A. S. Ellis, and F. T. Smith, "Trapping of air in impact between a body and shallow water," J. Fluid Mech. **611**, 365–394 (2008).

[60]F. T. Smith, "On the high Reynolds number theory of laminar flows," IMA J. Appl. Math. **28**, 207–281 (1982).

[61]I. Sobey, *Introduction to Interactive Boundary Layer Theory* (Oxford University Press, 2000).

[62]S. Kalliadasis and H.-C. Chang, "Drop formation during coating of vertical fibres," J. Fluid Mech. **261**, 135–168 (1994).

[63]R. J. Braun and A. D. Fitt, "Modelling drainage of the precorneal tear film after a blink," Math. Med. Biol. **20**, 1–28 (2003).

[64]F. T. Smith, "Finite-time break-up can occur in any unsteady interacting boundary layer," Mathematika **35**, 256–273 (1988).

[65]K. Langley, E. Q. Li, and S. T. Thoroddsen, "Impact of ultra-viscous drops: Air-film gliding and extreme wetting," J. Fluid Mech. **813**, 647–666 (2017).

[66]T. Hoksbergen, I. Baran, and R. Akkerman, "Rain droplet erosion behavior of a thermoplastic based leading edge protection system for wind turbine blades," IOP Conf. Ser.: Mater. Sci. Eng. **942**, 012023 (2020).

[67]R. Purvis and F. T. Smith, "Improving aircraft safety in icing conditions," in *UK Success Stories in Industrial Mathematics* (Springer International Publishing, 2016), pp. 145–151.

[68]M. Knoche, "Effect of droplet size and carrier volume on performance of foliage-applied herbicides," Crop Prot. **13**, 163–178 (1994).

[69]N. Laan, K. G. de Bruin, D. Bartolo, C. Josserand, and D. Bonn, "Maximum diameter of impacting liquid droplets," Phys. Rev. Appl. **2**, 044018 (2014).

[70]M. R. Moore, "Introducing pre-impact air-cushioning effects into the Wagner model of impact theory," J. Eng. Math. **129**, 6 (2021).